Research Square

Preprints are preliminary reports that have not undergone peer review.
They should not be considered conclusive, used to inform clinical practice,
or referenced by the media as validated information.

Angiotensin II-mediated neuroinflammation in the hippocampus contributes to heart failure-induced neuronal deficits and cognitive impairment in rats

Ferdinand Althammer
Georgia State University
Ranjan Roy
Georgia State University https://orcid.org/0000-0001-6234-8043
Matthew Kirchner
Georgia State University
Kathryn Whitley
Georgia State University
Steven Davis
Georgia State University
Juliana Montanez
Georgia State University
Hildebrando Ferreira-Neto
Georgia State University
Jessica Danh
Georgia State University https://orcid.org/0000-0001-7739-0287
Rafaela Feresin
Georgia State University https://orcid.org/0000-0003-0649-2774
Vinicia Biancardi
Auburn University https://orcid.org/0000-0001-7301-1702
Marise Parent
Georgia State University
Javier Stern (jstern@gsu.edu)
Georgia State University

Article

Keywords: microglial Angiotensin II, heart failure, cognitive decline

Posted Date: October 22nd, 2021

DOI: https://doi.org/10.21203/rs.3.rs-1000713/v1

License: This work is licensed under a Creative Commons Attribution 4.0 International License.
Read Full License

Angiotensin II-mediated neuroinflammation in the hippocampus contributes to heart failure-induced neuronal deficits and cognitive impairment in rats

Ferdinand Althammer[1]*, Ranjan K. Roy[1]*, Matthew K. Kirchner[1], Kathryn E. Whitley[2], Steven Davis[2], Juliana Montanez[1], Hildebrando Candido Ferreira-Neto[1], Jessica Danh[3], Rafaela Feresin[3], Vinicia Campana Biancardi[4, 5], Marise B. Parent[1,2] and Javier E. Stern[1,2#]

Affiliations: [1]Center for Neuroinflammation and Cardiometabolic Diseases, Georgia State University, GA, USA, [2]Neuroscience Institute, Georgia State University, GA, USA, [3]Department of Nutrition, Georgia State University, Atlanta, GA 30302, USA, [4]Anatomy, Physiology, & Pharmacology, College of Veterinary Medicine, Auburn University, Auburn, AL, USA, [5]Center for Neurosciences Research Initiative, Auburn University, Auburn, AL, USA.

*These authors contributed equally

[#]Corresponding author

Summary

The cellular mechanisms underlying cognitive impairments in heart failure (HF) remain unknown. Although HF-induced neuroinflammation and hypoxia in the hippocampus have been reported in humans and rodents, whether and how these processes are causally connected remains unexplored. Here we report that microglial Angiotensin II (AngII) signaling in the hippocampus is a crucial component in HF-induced neuroinflammation. We found microglial-specific upregulation of the AngII receptor AT1a that coincided with a hypoxic state, but preceded cytokine production. In addition to hippocampal apoptotic clusters, HF rats displayed progressive angiogenesis, migration of AT1a-positive microglia to blood vessels, and disruption of BBB integrity. Treatment of HF rats with the AT1 receptor antagonist losartan reversed neuroinflammation (but not hypoxia), apoptosis and cognitive impairments in HF rats. Taken together, we present here a novel mechanism by which microglial AngII signaling triggers a microglia-dependent neuroinflammatory cascade that contributes to neuronal apoptosis, hippocampal structure deterioration and cognitive decline.

Introduction

Heart failure (HF) is a debilitating disease affecting more than 64 million people worldwide[1]. In addition to impaired cardiovascular performance and associated systemic complications, most patients with HF suffer from depression[2] and/or substantial cognitive decline[3]. Multiple studies both in human patients and experimental animal models of HF have shed on into pathophysiological mechanisms known to contribute to cardiovascular dysfunction, cardiac necrosis[4,5] or inflammation[6], as well as elevated sympathohumoral activation[7], a hallmark of HF[4,8]. Conversely, the specific neural substrates and mechanisms contributing to emotional and cognitive decline in HF remain to be determined. The hippocampus plays a critical role in cognitive performance[9], including spatial, temporal and emotional memory[10]. Moreover, hippocampal structural and functional abnormalities as a result of normal aging[11] or in brain disorders such as Alzheimer's Disease[12] have been shown to contribute to cognitive deficits. Importantly, recent studies also showed shrinkage and reductions in hippocampal volume in HF both in rats[13] and humans[14]. Taken together, these previous studies support the hippocampus as a likely brain substrate contributing to cognitive deficits in HF.

Two major pathological events have been suggested as likely candidates contributing to neurological dysfunction in HF. Firstly, it is well-established that myocardial infarction leads to insufficient oxygen supply to the brain and subsequent hypoxia[15,16]. Secondly, recent studies support neuroinflammation as a common finding in numerous brain regions of HF rats[8,17-19]. Whether these two pathological factors are causally interrelated, and what their relative contribution to cognitive deficits in HF is remains largely unknown.

Neuroinflammation is a process regulated by microglial and astrocytic interactions[20]. Microglia, the resident macrophages of the brain parenchyma, monitor and protect neurons under normal conditions[21]. Conversely, sustained microglial activation during pathological conditions induces a neurotoxic astrocyte phenotype[20], which eventually results in neuronal death. In HF, overactivation of the renin-angiotensin system has been shown to play a critical role in sympathohumoral activation and the associated cardiovascular detrimental effects[22-24]. Importantly, the circulating peptide angiotensin II (AngII) is recognized as a potent proinflammatory molecule[25], and several studies support a contribution of AngII and its AT1a receptor to hypothalamic neuroinflammation and sympathohumoral activation in HF[8,19,26-30] and other related cardiovascular diseases such as hypertension[31,32]. Given this, and the fact that AT1a receptors are also expressed in hippocampal microglia[33], we aimed to test the overarching hypothesis that AngII/AT1a-driven microglial activation contributes to hippocampal neuroinflammation, neuronal death and cognitive deficits in HF.

The ischemic HF rat model is a widely accepted model than replicates the cardiac, systemic and neurohumoral pathology observed in patients[34]. Moreover, we[35] and others[36] recently showed that HF rats displayed various cognitive and emotional deficits reported in humans, supporting that this model is well-suited to also study mechanisms underlying HF-induced cognitive and emotional impairments. Using this model, we report that HF rats with reduced ejection fraction (EF) displayed long-lasting microglial activation in both ventral (VH) and dorsal hippocampus (DH). We found hippocampal morphometric microglial changes

supportive of a pro-inflammatory state that strongly correlated with higher expression of proinflammatory cytokines. These pro-inflammatory changes correlated with the progression and severity of the disease. We found evidence for altered hippocampal neuronal excitability and substantial hippocampal apoptosis in HF rats. Intriguingly, we observed an increased number of vessel-associated microglia, elevated expression of hypoxia markers, angiogenesis and compromised hippocampal blood-brain barrier (BBB) integrity in HF rats. Most of these changes correlated with an increased expression of AT1R mRNA levels in hippocampal microglia. Importantly, treatment of HF rats with an AT1R antagonist improved all neuroinflammation-associated parameters, without affecting however the hippocampal hypoxic state. Finally, AT1R blockade ameliorated cognitive deficits in HF rats. Collectively, our results highlight a novel mechanism of AngII-AT1aR-mediated hippocampal microglial activation in HF, which progresses over time and has detrimental effects on hippocampal function and hippocampal-dependent memory.

Results

Heart failure induces a pro-inflammatory microglial phenotype in the hippocampus

To assess potential microglia morphological differences between sham and HF rats, we stained brain sections containing DH and VH for the microglial marker IBA1 (n=8 for both groups, **Fig. 1a, Extended Fig. 1a-f**). We found larger microglia somatic volumes in HF rats (**Fig. 1b,c**[37]), which could be indicative of a pro-inflammatory microglial phenotype. This was further confirmed using an Imaris-assisted microglia morphometry approach[17] that showed significant changes in microglia surface area, cell volume, and filament length that are consistent with a proinflammatory phenotype (**Fig. 1d-f**). Interestingly, these changes were dependent on the progression of the disease, with animals at later stages of HF displaying more profound changes in microglial morphology. We recently reported lack of microglial morphological changes in the somatosensory cortex (S1BF) of HF rats[17]. To further confirm that microglial morphology changes in HF are not a brain-wide phenomenon, we analyzed also here the prelimbic cortex (PLC) and found no difference between sham and HF rats (**Extended Fig. 1g-i**). To obtain more detailed information about changes in microglial morphometry, we created heatmaps of 256 randomly selected microglia (32 per animal) that display the maximum length and Sholl values for each microglia for both Sham and HF rats (**Fig. 1g, h**). On average, microglia from HF rats displayed a reduced reach (i.e. maximum extension of filaments) and diminished maximum complexity (peak Sholl value). Next, we compared between both groups the proportions of microglia that were considered pro-inflammatory using our previously established conservative threshold ([17], peak Sholl value <10). In sham rats, we found 14.9% and 15.3% (in VH and DH, respectively) of all microglia to display a pro-inflammatory profile, while the value was increased in HF rats (**Fig. 1i, j**; 41.2% and 36.2% for VH and DH, respectively). No such changes were observed in the PLC, consistent with our initial findings (**Extended Fig. 1j, k**). Importantly, we found a significant negative correlation between the degree of microglia cell activation and the corresponding rat echocardiography EF value (**Fig. 1k, l**), suggesting that the microglial status within the hippocampus is dependent on the severity of cardiac compromise in HF. The HF-induced decrease in microglia morphology complexity was further confirmed by Sholl analysis (**Fig. 1m**). Counting of microglia revealed no differences in the total number or

density of microglia cells between the two groups, indicative of lack of microglia cell proliferation during HF (**Fig. 1n)**. Assessment of mRNA transcripts via qPCR revealed a significant increase in several neuroinflammation-associated genes within the VH and DH (**Fig. 1o)**, but not in the PLC **(Extended Fig. 1l)**. Taken together, these findings suggest that hippocampal microglia undergo a morphological transition towards a pro-inflammatory phenotype in HF which is progressive in time, and dependent on the severity of the disease.

Morphological changes in microglia correlate with cytokine mRNA levels in HF rats

Cytokines such as C1q, TNFα and IL1β play an important role in microglia-to-microglia communication and are pivotal to microglia-mediated maintenance of a pro-inflammatory state[20]. To determine whether microglial morphological changes correlated with changes in the levels of cytokine expression, we combined immunohistochemistry (IHC) against IBA1 with the RNASCope hybridization to measure cytokine expression and correlated the degree of microglial pro-inflammatory morphological changes and the amount of cytokine mRNA expressed within individual microglia cells in sham and HF rats (**Fig. 2a-g, Extended Fig. 2a-e**). We found a robust and significant negative correlation between IL1β and TNFα mRNA levels with microglial complexity, while the correlation with C1q was less prominent though still significant.

A core feature of neuroinflammation is the intricate interaction between microglia and astrocytes. Microglia release C1q, TNFα and IL-1α to activate astrocytes, which in turn become neurotoxic (A1 phenotype) and induce apoptosis in neighboring neurons in affected brain areas[20]. To investigate whether HF induced a morphological transition of astrocytes towards a pro-inflammatory A1 phenotype, we stained astrocytes using GFAP and glutamine synthetase (GS) as markers which predominantly stain astrocytic processes and astrocyte soma, respectively (**Fig. 2h, i**). We found that HF astrocytes in the VH and DH, but not the PLC, had substantially increased soma volume and visible swelling of GFAP-labeled processes, indicative of a hypertrophic phenotype[38] and reactive astrocytes[39] (**Extended Fig. 2f-h**). In line with this, we found lower levels of neuroprotective A2- and higher levels of neurotoxic A1-related mRNA transcripts in the hippocampus of HF rats (**Fig. 2j***)*. Similar to microglia changes, we did not observe changes in astrocyte morphology (**Extended Fig. 2h),** nor an increase in the number of astrocytes in the PLC (**Extended Fig. 2i**). Taken together, these findings are consistent with the previously described interaction of microglia and astrocytes during neuroinflammation[20,40], and support that in addition to a microglia proinflammatory state, the hippocampus of HF rats shows evidence for an astrocytic shift from a neuroprotective to a neurotoxic state.

Evidence for hippocampal apoptosis in HF rats

To probe for potential neuroinflammation-induced apoptosis in the hippocampus of HF rats, we performed a TUNEL assay to assess apoptotic levels in the DH and VH of sham and HF rats. This study was done at two different time points (6w and 16w post HF) to be able to discriminate between early and late apoptosis in our HF model (**Fig. 3a, b, Extended Fig. 3 a, b**). We observed frequent apoptotic clusters

in both DH and VH of HF rats, while those clusters were almost entirely absent in sham rats (**Fig. 3 c, d**). To corroborate these findings, we stained brain sections of sham and HF rats with a cleaved caspase-3 (cCasp3) antibody and found significant more apoptotic clusters at 6w and 16w post HF surgery in the hippocampus (**Fig. 3e-j**). Interestingly, we observed a reduction in cell number at 16w, but not 6w post HF surgery (**Fig. 3g, j**), suggesting continued apoptosis that manifests in significant decreases in cell numbers only in later stages of HF. In addition to the observed apoptotic clusters and reduced cell number, we also found significant thinning of pyramidal cell layers both in the DH and VH of HF rats (**Extended Fig. 3 c-e**), which is in line with previous reports of hippocampal shrinkage in HF rats[13].

To further assess hippocampal neuronal damage during HF we patched *ex vivo* pyramidal neurons in dorsal CA1 in both sham and HF rats (n= 11 neurons/ 3 rats and 9 neurons/3 rats respectively) and assessed changes in membrane excitability and firing discharge properties (**Fig. 3 k-o, Extended Fig. 3f**). While resting membrane potential was similar between CA1 neurons in sham and HF, we observed a significantly decreased input resistance which was evident as a decreased slope in the current/voltage plots (**Fig. 3l**). Moreover, we found a significantly diminished input/output function in CA1 neurons in HF rats (i.e. decreased number of evoked action potentials per stimulation, **Fig. 3o**). AP amplitude, AP threshold, AP half-width, peak AHP amplitude, sAHP amplitude, or AHP decay *tau* did not differ between sham and HF rats (**Extended Fig. 3f**). Taken together, these findings indicate an early onset of HF-induced hippocampal apoptosis, along with a blunted overall neuronal excitability and decreased ability to fire action potentials in response to an incoming stimulus.

Upregulation of hippocampal Hif1/2α and Angiogenesis during HF

Myocardial infarction with reduced ejection fraction results in a hypoxic environment that can have far-reaching consequences on brain vascularization, metabolism and ultimately brain function[41-44]. However, whether tissue hypoxia and/or pathological angiogenesis occurs in the hippocampus of HF rats, and whether it is mechanistically linked to the neuroinflammatory process during this condition remains unknown. Thus, we performed qPCR time series for Hif1α and Hif2α, two widely used hypoxia markers, at 6-, 8- and 12-weeks post HF. We found a significant increase in both Hif1α and Hif2α in the VH and DH of HF rats. Intriguingly, while the magnitude of the increase in Hif1α levels diminished over time, Hif2α kept increasing over time (**Fig. 4a, b**). In line with previous studies showing that Hif2α promotes pathological angiogenesis under various conditions[45,46], we assessed for changes in hippocampal vascular density in sham and HF rats at two different time points (6 and 12-weeks post HF) (**Fig. 4c-h**). We observed a prominent and progressing increase in vascularization in both DH and VH of HF rats (**Fig. 4e, f, h**), as well as in the somatosensory cortex, paraventricular nucleus of the hypothalamus (PVN) and central nucleus of the amygdala (CeA) (**Extended Fig. 4a-e**). Finally, we analyzed vessel branching points for each animal and found significantly higher numbers of vessel branching points in HF rats, with a progressive increase over time (**Extended Figure 4f**). These findings support hypoxia and hyper-vascularization in multiple brain regions in rats with HF.

AT1aR expression in hippocampal microglia is linked to microglial activation during HF

Overactivation of the renin-angiotensin system (RAS) is a hallmark of HF, and disturbed angiotensin II (AngII) signaling is thought to underlie many of the pathophysiological findings and symptoms associated with early and late HF stages[8,19,28]. AngII is a pro-inflammatory neuropeptide[25] and we recently reported that AngII type 1a receptors (AT1aR) are present in hypothalamic microglia[30,31,47], while others have shown the same in hippocampal microglia[33]. Thus, we first performed non-cell type-specific qPCR to determine whether AT1aRs were upregulated in HF rats. Indeed, we found a time-dependent, progressive increase of AT1aRs both in the DH and VH of HF rats when compared to age-matched sham controls (**Fig. 5a**). Interestingly, we could confirm these findings in PVN and CeA, where we previously reported microglial activation[17], but not the somatosensory cortex or PLC (**Extended Fig. 5a**). To determine whether the degree of AT1aR expression was linked to microglial deramification, we performed RNAScope for AT1aR mRNA in combination with IHC staining against IBA1 (**Fig. 5b-f**) and we analyzed the peak Sholl values in AT1aR -negative and AT1aR-positive microglia. We found that AT1aR positive microglia were significantly less complex than their AT1aR-negative counterparts, suggesting a potential role of AT1aR in regulation of microglial morphology and functional state (**Fig.5e**). In addition, we observed a drastic increase (6-fold) in the number of AT1aR mRNA positive microglia in both DH and VH of HF rats (**Fig. 5f, g**), as well as a significant 1.4-fold increase in AT1aR mRNA expression in hippocampal microglia of HF rats (**Extended Fig. 5b).** In hippocampal neurons, a 2.8-fold increase in AT1aR mRNA expression was also observed in HF rats (**Extended Fig. 5c-e**), however, unlike hippocampal microglia, the total number of AT1aR mRNA-positive neurons in HF rats did not increase (**Fig. 5f**). We did not find evidence for AT1aR receptors in hippocampal astrocytes in sham or HF rats (**Extended Fig. 5f**).

Following our findings showing increased cytokine production and microglial ATa1R upregulation, we sought to better understand the time course of these concomitantly occurring phenomena. Thus, we performed qPCR at a very early stage (10 days post HF surgery) for IBA1, cytokines and AT1aR mRNA (**Fig. 6 a, b**). We not only found elevated levels of AT1aR mRNA at this stage, but also observed that the increase in AT1aR mRNA preceded the increases in IBA1, TNFα, IL1β and IL6 (**Fig. 1**). Thus, it is tempting to propose that AT1aR-mediated activation of hippocampal microglia in HF rats contributes to the induction of the observed morphological changes and subsequent induction of microglial cytokine production.

Increased number of vessel-associated, AT1aR-positive microglia during HF

A recent study showed that during systemic inflammation microglia migrate towards blood vessels and promote BBB stability through Claudin-5[48]. However, upon sustained inflammation, microglia begin to phagocytose astrocytic AQP4-positive endfeet in a CD68-dependent manner, thereby compromising BBB integrity[48]. Inspired by this discovery, we sought to investigate potential changes in hippocampal vessel-associated microglia following myocardial infarction. Thus, we combined IHC against IBA1 and AQP4 and analyzed the number of vessel-associated microglia in Sham and HF rats in VH and DH. Intriguingly, we found a stark increase in the number of vessel-associated microglia, accompanied by a decrease in parenchymal microglia (DH and VH combined, **Fig. 7a-c**). Interestingly, we observed a substantial variation

in shape and AQP4-positive contact points of vessel-associated microglia, which prompted us to further characterize them (**Fig. 7d, Extended Fig. 6a**). We categorized vessel-associated microglia as Type I (microglial filaments contacting the vessel), Type II (partial microglial soma contacting the vessel) and Type III (extensive microglial soma contacting the vessel). We found that the relative incidence of Type I-III microglia varied between Sham and HF rats (**Fig. 7e**), with Type I predominating in Sham rats but Type III predominating in HF rats. Interestingly, Type III microglia in HF rats frequently protruded into blood vessels (**Fig. 7f, Extended Fig. 6b**), which is in line with observations recently been made by another group[48]. Vessel protrusion by microglia was much less frequently observed in Sham rats (**Extended Fig. 6c).** Finally, we performed RNAScope *in situ* hybridization for AT1aR mRNA in combination with AQP4 and IBA1 IHC, and found that the vast majority of Type III vessel-associated microglia in Sham and HF rats were AT1aR-positive (**Fig. 7g-i**). Based on these findings, we propose that AT1aRs not only promote microglia activation in the hippocampus, but potentially stimulate their migration towards blood vessels and disruption of BBB integrity.

Increased BBB permeability and co-localization of circulating AngII with microglia in HF rats

Given the profound changes in microglial migration, hypoxia, angiogenesis and AT1aR upregulation (**Figures 4-6**), we hypothesized that a compromised BBB could be a plausible mechanism contributing to the concomitantly-occurring phenomena[49,50]. As soon as 2-4 weeks post HF surgery, we found significantly larger leakage of intravascularly delivered FITC10 in the DH, VH and PVN, (but not somatosensory cortex or PLC) of HF rats compared to Sham rats (**Fig. 8 a-c, Extended Fig. 7a-d**). Three-dimensional reconstruction of blood vessels and extravasated dyes revealed that FITC predominantly accumulated at what seemed to be neuronal/cellular surfaces (**Fig. 8b**). We previously reported that AngII gains access to the CNS in a hypertensive rat model, and specifically co-localizes with microglia[31]. Thus, we hypothesized that a similar mechanism could underlie the HF-induced, AT1aR-driven neuroinflammation. Indeed, following intravascularly delivered fluorescently-labeled $AngII_{fluo,,}$ we found a significantly higher degree of IBA1-positive microglia cells displaying bound leaked $AngII_{fluo}$ in HF rats compared to Sham rats (**Fig. 8d, e, Extended Fig. 7e**). In addition, we found significant larger amounts of parenchymal $AngII_{fluo}$ in HF rats than Sham rats (**Extended Fig. 7f**), again corroborating our findings of increased BBB permeability and subsequent leakage. Interestingly, the average amount of $AngII_{fluo}$ taken up by HF microglia was 1.8-times higher than in Sham animals (**Extended Fig. 7g**), which could potentially be explained by the enrichment of AT1aRs (**Extended Fig. 5b**) in HF microglia. Finally, we aimed to determine whether $AngII_{fluo}$-labeled microglia were vessel-associated. To this end, we co-infused animals with Rho70 to label blood vessels and found that the vast majority of $AngII_{fluo}$-positive microglia was vessel-associated in HF rats (**Fig. 8f, g, Extended Fig. 7h**).

Blockade of AT1Rs improves neuroinflammation, apoptosis and cognitive impairment in HF rats

Based on the results above suggesting a causal link between HF-induced exacerbated microglial AngII signaling, astrocyte activation, elevated cytokine levels and apoptosis (**Figs. 1-3**), we hypothesized

AT1aRs mediated these effects, and thus predicted that blocking AT1R-mediated signaling would ameliorate these pathological alterations. In addition, we were interested to determine whether this treatment could reverse our recently reported cognitive impairments in HF rats[35]. To this end, we randomly allocated HF rats to be given either normal drinking water or water containing the AT1R blocker losartan[31] (20 mg/kg/day) for 12 weeks after the myocardial infarction. While losartan did not affect cardiac function (**Extended Fig. 8a**), it did significantly decrease both systolic and diastolic blood pressure (**Extended Fig. 8b, c**), supporting the efficacy of the treatment[30]. In addition, losartan did not affect weight gain (**Extended Fig. 8d**) nor total water consumption (**Extended Fig. 8e**). We found that losartan significantly reduced mRNA levels for IBA1, GFAP, IL-1, IL-6 and TNF-α, but not AT1aR, Hif-1α or Hif-2α in the VH and DH (**Fig. 9a, b**). We also found that losartan significantly reversed previously observed changes in microglia morphology including cell volume, surface area and filament length in both hippocampal subdivisions (**Fig.9c-f**). In addition, losartan almost entirely reversed the previously observed changes in astrocyte morphology (**Extended Fig. 8f**). Importantly, losartan also significantly diminished cCasp3 staining both in the VH and DH (**Fig. 9g, h**). In addition, we found than losartan significantly decreased the number of vessel-associated microglia (**Extended Fig. 8g, h**). Finally, losartan almost entirely reversed the earlier described HF-induced shift (**Fig. 7**) in Type I-III microglia subtypes (**Extended Fig. 8i**).

We recently reported that, compared to sham rats, HF rats displayed signs of spatial and emotional memory impairments[35] both of which are associated with altered hippocampal function[51,52].To determine whether AT1aR-induced neuroinflammation contributed to these effects, we repeated the spontaneous alternation and inhibitory avoidance tests (IA) in HF and losartan-treated HF rats (**Fig. 9i**). We found that losartan-treated rats displayed significantly more percent alternations (**Fig. 9j**), suggestive of improved spatial working memory. Although losartan affected the sequence of arm entries (i.e., percent alternation), it did not affect the number of arms the rats entered in the maze (**Fig. 9k**), thereby ruling out that the observed behavioral changes were merely a result of changes in activity levels. Losartan-treated HF rats also had significantly higher retention latencies during the IA memory test, suggesting that it improved emotional memory (**Fig. 9l**). Of note, there were no differences in the training latencies (**Fig. 9m**), further supporting the interpretation that losartan did not affect activity levels. Taken together, these findings suggest that blocking AT1R-mediated AngII signaling partially prevents neuroinflammation and subsequent apoptosis, thereby reversing cognitive impairments observed in HF rats.

Discussion

A growing body of clinical studies supports a high degree of comorbidity between cardiovascular diseases and cognitive decline[53-55]. In fact, 20-40% of all HF patients develop major depression and elevated anxiety[2,53,54,56], along with memory-associated symptoms, which usually appear later than the cardiovascular and autonomic-related symptoms[3]. These cognitive and mood disorders have also been observed in experimental animal models of HF, including the rat and mouse left coronary ligation model[57-59]. Still, the mechanisms underlying HF-induced cognitive impairments remain largely unexplored. In our current study, we focused on the hippocampus, given that normal hippocampal function is paramount for

mood and memory, and that alterations in hippocampal signaling have been linked to cognitive decline, depression and anxiety[11,60]. In fact, hippocampal shrinkage and cell loss after HF have been observed in rats and humans[13,14]. In addition, cognitive impairment in HF rats has been recently demonstrated by our group[35] and others[36].

Microglia, the resident immune cells of the CNS, are highly dynamic cells that surveil the brain state and respond to injury by migration and substantial changes in cellular morphology[61], leading to a pro-inflammatory state and secretion of cytokines. As part of this process, microglia directly interact with astrocytes via cytokine signaling to further promote the neuroinflammatory cascade, eventually resulting in neuronal damage and death[20,40]. Using our recently developed morphometric profiler to assess microglial morphology at various stages in sham and HF rats[17], we found significant microglial process retraction, somatic swelling and reduction of surface area, all of which are in line with a pro-inflammatory microglial phenotype[17,62,63]. Intriguingly, we not only observed time-dependent microglia morphological changes during the progression of the disease, but also brain region-specific changes, highlighting potential brain differences in susceptibility and resilience to HF-induced neuroinflammation. Moreover, these changes were dependent on the severity of cardiac compromise in HF. The robust and significant negative correlation we report between cytokine level expression (e.g. IL1β and TNFα) with microglial complexity markers, further support the microglia pro-inflammatory status in the hippocampus of HF rats.

A core feature of the neuroinflammatory process is the intricate interaction between microglia and astrocytes. Consistent with our previous findings in the PVN and amygdala[17], we report here swelling of astrocyte processes in DH and VH, as well as an astrocytic shift from a neuroprotective to a neurotoxic state. It was previously demonstrated that such an astrocyte shift during sustained neuroinflammation promotes neuronal death and apoptosis[20,64]. In line with this, but in the context of a systemic cardiovascular disease state, we show evidence for hippocampal apoptosis (as early as 6 weeks post HF surgery), along with diminished cell counts and shrinkage of pyramidal cell layers. Moreover, ex vivo electrophysiological recordings obtained from CA1 pyramidal neurons in sham and HF rats showed a significantly blunted membrane excitability as well as blunted input/output function in the later. While the precise mechanisms leading to these changes in intrinsic membrane properties remain to be determined, these studies support an overall blunted ability of CA1 pyramidal during HF to process an incoming input to generate a proper action potential firing output. Altogether, these findings are consistent with the notion of neuroinflammation-induced neuronal dysfunction and neurotoxicity[20], and suggest that HF could lead to drastic and long-lasting pathological alterations in brain structure and function.

Work from our lab[28,31,32,65] and others[8,19,24,26,27] have shown that the pro-inflammatory peptide AngII is linked to both neuroinflammation and autonomic changes in HF and hypertension. In addition, a recent study showed that systemic administration of AngII induced neuroinflammation in the mouse hippocampus[66]. Still, whether endogenous AngII contributes to hippocampal neuroinflammation and hypoxia in HF remained unknown. Several pieces of evidence from our study support this to be the case: i) a gradual and progressive increase of AT1aR mRNA in HF rats prior to elevated cytokine mRNA levels, ii) a 6-fold increase in AT1aR-positive microglia in HF rats and iii) virtually all deramified microglia in HF rats

were AT1aR-positive. Finally, a causal link between AngII-AT1aR and neuroinflammation is more compellingly supported by the fact that treating HF rats with the AT1R antagonist losartan substantially reversed numerous microglial morphometric changes and the elevated cytokine levels observed in non-treated HF rats. Importantly, AT1R blockade also significantly diminished hippocampal apoptosis, further supporting a mechanistic role for AngII-AT1R in mediating neuroinflammation and neuronal death in the hippocampus of HF rats. These results are in line with a previous study showing that candesartan (another AT1R blocker) ameliorated brain inflammation following LPS injection[67]. Finally, it is worth highlighting that neuroinflammatory markers were evident only in brain regions where an expression/upregulation of AT1aR was observed (e.g., hippocampus/PVN, but not PLC or SSC). Thus, the brain region specificity of the neuroinflammatory response during HF could be dependent, at least in part, on a concomitant region-specific upregulation of AT1aRs in this condition. Clearly, additional work is needed to more conclusively asses this. An important caveat to take into consideration is that losartan blocks AT1R signaling in all cells, not just microglia. Thus, a contribution of AT1R-expressing neurons to neuroinflammation and apoptosis cannot be ruled out entirely. Finally, we observed a losartan-induced reduction in astrocytic soma volume as well as a reduction in GFAP mRNA, even though we found no evidence for astrocytic AT1aR receptors. These results in also in line with previous findings showing that astrocyte signaling in neuroinflammation is downstream to activated microglia[20].

It was recently showed that during systemic inflammation microglia migrate towards blood vessels and promote BBB stability through Claudin-5[48]. However, upon sustained inflammation, microglia begin to phagocytose astrocytic AQP4-positive endfeet in a CD68-dependent manner, thereby compromising BBB integrity[48]. In this context, we found a robust increase in the number of vessel-associated microglia, accompanied by a decrease in parenchymal microglia in HF rats. We categorized vessel-associated microglia as Type I (microglial filaments contacting the vessel), Type II (partial microglial soma contacting the vessel) and Type III (extensive microglial soma contacting the vessel). Importantly, we found a shift from Type1 to Type 3 microglia in HF, with AT1aRs selectively expressed in the later. Interestingly, a similar categorization of vessel-associated microglia was recently reported in the somatosensory cortex of mice[68] where parenchymal and vessel-associated microglia represent interchangeable populations, allowing the recruitment of microglia from one pool to the other under normal conditions in the healthy brain. To our knowledge however, this represents the first account of recruitment of activated microglial towards a vascular pool during a pathological condition. Moreover, the fact that losartan prevented this recruitment supports the hypothesis that AngII-AT1aRs not only promote microglia activation in the hippocampus during HF, but that this signaling unit could also stimulate their migration towards blood vessels to promote disruption of BBB integrity. To test whether this was the case, we used a well-established approach to quantitatively assess BBB permeability using intravascular infusions of fluorescently-labeled dyes[31]. Our results showed significant BBB leakage in the DH and VH (as well as PVN, but not in the somatosensory cortex or PLC) in HF rats, which was sufficient enough to allow circulating AngII to leak into the hippocampal parenchyma. Interestingly, and in line with a previous study in hypertensive rats[31] we found leaked AngII to be bound predominantly to microglial cells. Taken together, these results, along with the fact that AT1R

blockade prevented BBB leakage in HF rats, provide compelling evidence that AngII-AT1aR activation during HF contributes to microglial cell activation and recruitment into a vascular pool, leading ultimately to disruption of BBB integrity. These findings are in line with a recent study from our lab showing the involvement of AT1Rs in BBB disruption in hypertensive rats[69].

Altogether, the above data strongly support an AngII-AT1aR-mediated pro-inflammatory microglia state, an astrocytic shift from neuroprotective to neurotoxic phenotype, neuronal dysfunction and apoptosis, and BBB disruption in HF rats. Importantly, these factors have been shown to contribute to cognitive decline and mood disorders in neurodegenerative conditions[70-72]. We recently reported that, compared to sham rats, HF rats displayed signs of spatial and emotional memory impairments[35], both of which are associated with altered hippocampal function[51,52]. Importantly, we report here that losartan-treated HF rats showed significant cognitive improvements compared to their non-treated counterparts, as shown by improved performance both during the spontaneous alternation and the inhibitory avoidance testing, while the number of arm entries and training latencies were not affected. These findings are highly relevant from a clinical standpoint and suggest that exacerbated AngII-AT1aR signaling in the hippocampus of HF rats is a pivotal mechanism driving the cognitive impairment observed after HF. We selected to deliver losartan orally, to mimic the conventional clinical route of administration in patients. We acknowledge however that this limits our ability to determine the site of action of this drug to mediate the reported effects. Still, we believe this limitation is mitigated by the fact that AT1aRs were upregulated in very selective brain regions, particularly the hippocampus, a well-established brain region involved in memory and cognitive functions.

In addition to neuroinflammation, hypoxia, due to the overall compromised cardiac output and oxygen tissue perfusion[15,16], stands as another key pathological mechanisms in HF. However, to what extent hypoxia is mechanistically linked to neuroinflammation, and whether it contributes to cognitive deficits in HF is unknown. Our findings showing increased expression of Hif1α and Hif2α, along with hypervascularization, (a well-established compensatory response to tissue hypoxia[73]) in all brain regions explored (DH and VH, as well as somatosensory cortex, PVN and amygdala) support indeed brain hypoxia in HF rats. Intriguingly however, while AT1R blockade almost completely reversed most, if not all of the neuroinflammatory endpoints, the hypoxia markers Hif1α and Hif2α remained elevated. This suggests that AT1aR-mediated neuroinflammation and hypoxia are two relatively independent pathophysiological processes during HF, and that the former is a key contributor to cognitive deficits in this condition, at least at the time points of the disease assessed in the present study. A schematic summary of the proposed mechanisms leading to AngII-AT1R-mediated contribution to cognitive deficits in HF is shown in **Fig. 10**. Overall, our results provide new evidence to support the hippocampal AngII-ATa1R signaling cascade as a novel therapeutic target to combat HF-induced cognitive decline and memory impairment.

Materials and methods

All experiments were approved by the Georgia State University Institutional Animal Care and Use Committee (IACUC) and carried out in agreement with the IACUC guidelines. At all times, animals had *ad*

libitum access to food and water and all efforts were made to minimize suffering and the numbers of animals used for this study.

Animals

We used male Wistar rats (5-7 weeks old at HF surgery, 180-200g, Envigo, Indianapolis, IN, USA) for all experiments (n=151). Rats were housed in cages (2 per cage) under constant temperature (22 ± 2°C) and humidity (55 ± 5%) on a 12-h light cycle (lights on: 08:00-20:00).

Heart failure surgery and Echocardiography

As previously described[74] HF was induced by coronary artery ligation surgery. Animals were anaesthetized using 4% isoflurane/oxygen and intubated for mechanical ventilation until the end of the surgery. To exteriorize the heart, we performed a left thoracotomy and the ligation was performed on the main diagonal branch of the left anterior descending coronary artery. Animals received buprenorphine SR-LAB (0.5 mg/kg, S.C.; ZooPharm, Windsor, CO, USA) before the surgical procedure to minimize postsurgical pain. Sham animals underwent the same procedure except the occlusion of the left coronary artery. One to 4 weeks after the surgery, we performed transthoracic echocardiography (Vevo 3100 systems; Visual Sonics, Toronto, ON; Canada) under light isoflurane (2-3%) anesthesia to assess the EF and confirm the development of HF. We obtained the left ventricle internal diameter and the left diameter of the ventricle posterior and anterior walls in the short-axis motion imaging mode to calculate the EF. The myocardial infarct surgery typically results in a wide range of functional HF, as determined by the EF measurements. Rats with EF<50% were considered as HF and the average EF was 85.84 ± 2.24 % for Sham rats and 31.16 ± 3.46 % for HF rats.

Immunohistochemistry

Following pentobarbital-induced anesthesia (Euthasol, Virbac, ANADA #200-071, Fort Worth, TX, USA, Pentobarbital, 80mg/kgbw, i.p.), rats were first perfused at a speed of 20mL/min with 0.01M PBS (200mL, 4°C) through the left ventricle followed by 4% paraformaldehyde (PFA, in 0.3M PBS, 200mL, 4°C), while the right atrium was opened with an incision. Brains were post-fixed for 24 hours in 4% PFA at 4°C and transferred into a 30% sucrose solution (in 0.01M PBS) at 4°C for 3-4 days. For immunohistochemistry, 40 µm slices were cut using a Leica Cryostat (CM3050 S) and brain slices were kept in 0.01M PBS at 4°C until used for staining. Brain slices were blocked with 5% Normal Horse Serum in 0.01M PBS for 1h at room temperature. After a 15-min washing in 0.01M PBS, brain slices were incubated for 24h in 0.01M PBS, 0.1% Triton-X, 0.04% NaN_3 containing different antibodies: 1:1000 of anti-IBA1 (polyclonal rabbit, Wako, 019-19741, Lot: CAK1997), 1:1000 anti-glutamine synthetase (monoclonal mouse, Merck Milipore, MAB 302, clone GS-6), anti-GFAP (goat polyclonal, abcam, ab53554), anti-AQP-4 (polyclonal rabbit, Alomone labs, AQP-004) at room temperature. Following 15-min washing in 0.01M PBS, sections were incubated in 0.01M PBS, 0.1% Triton-X, 0.04% NaN_3 with 1:500 Alexa Fluor 488/594-conjugated donkey anti-rabbit/goat/mouse (Jackson ImmunoResearch, 711-585-152, 705-585-147, 715-545-151) for 4 hours at RT. Brain slices were

washed again for 15 mins in 0.01M PBS and mounted using antifade mounting medium (Vectashield with DAPI, H-1200B/H-1500).

RNAScope in situ hybridization

RNAScope reagents were purchased from acdbio (PN320881). Nuclease-free water and PBS were purchased from Fisher Scientific. Brains were processed as described under ***Immunohistochemistry*** using nuclease-free PBS, water, PBS and sucrose. We followed the manufacturer's protocol with a few modifications: 1) Immediately after cryosectioning, sections were washed in nuclease-free PBS to remove sucrose and OCT compound. 2) Hydrogen peroxide treatment was performed with free floating sections prior to slice mounting. 3) Sections were mounted in nuclease-free PBS at room temperature. 4) Pretreatment with Protease III was performed for 20 minutes at room temperature. 5) No target retrieval step was performed. For analysis, microglia were considered mRNA-positive if they displayed three or more fluorescently-labeled voxels within the respective microglia soma.

Confocal microscopy and 3D IMARIS analysis

Confocal images were obtained using a Zeiss LSM 780 confocal microscope (1024x1024 pixel, 16-bit depth, pixel size 0.63-micron, zoom 0.7). Unless indicated otherwise, we used 6-8 sections per animal for the assessment of various parameters (microglia classification, microglia morphology, microglia number etc.). For each animal, averages were calculated and the respective dots in the graphs represent the average value for each parameter for each animal. For the three-dimensional reconstruction 40µm-thick z-stacks were acquired using 1µm-steps. Three-dimensional reconstruction of microglia, astrocytes or axons was performed as previously described[17]. Image processing, three-dimensional reconstruction and data analysis were performed in blind to the experimental conditions. In Sham rats, we found no differences in microglial morphology in the DH and VH subdivisions CA1, CA2, CA3 or dentate gyrus and thus pooled all microglia into VH and DH (**Extended Fig. 1c-f)**. For the quantification of mRNA transcripts and the subsequent correlation with microglial morphology, spheres precisely engulfing the microglial soma were manually placed on individual microglia as described previously [75]. The fluorescent intensity within the respective spheres was measured and then correlated with microglial complexity assessed via Sholl analysis. To assess cytokine mRNA levels in neurons, we selected IBA1-negative cells that were located within the pyramidal cell layers of VH and DH. For the analysis of microglia-specific uptake of $AngII_{fluo}$, each microglia was assessed individually in Imaris, and green $AngII_{fluo}$ voxels were selected manually and summed for total $AngII_{fluo}$ volume in each microglia.

Analysis of cellular density, area fraction, signal intensity, vessel bifurcations and vessel volume

Cellular density (microglia or astrocytes) was assessed blindly using the cell counter plugin in Fiji. for each animal, 8-10 brain sections were used for analysis, if not indicated otherwise. Area fraction and signal intensity were assessed using the Adjust→Threshold function in Fiji, and every image was adjusted individually for optimal yield and overlap with original fluorescence. Following thresholding, area fraction

and density were measured using the Set Measurements→Measure function in Fiji. Area fraction is represented in %, while signal intensity is represented in AU in the respective graphs. For the quantification of pathological hypervascularization, vessel bifurcations using AQP4 staining was assessed manually while being blind to the experimental conditions. Collapsed, maximum projections (40µm) images were used and each apparent bifurcation (here defined as a clearly visible delineation/junction from the main vessel) was assessed manually in Fiji using the cell counter plugin. AQP4 vessel volume was analyzed using the above-described three-dimensional reconstruction for AQP4 surface area in Imaris. We used 6-8 confocal z-stacks (40µm depth) for each animal and vessel volume for each individual brain section represents the total volume sum of all vessels within that image. The average vessel volume for each animal was then calculated by dividing the total vessel volume for all images by the number of images.

Analysis of pyramidal layer thickness

For the analysis of DH and VH pyramidal layer thickness in Sham and HF rats, brain sections (40µm) were collected in sets for each individual animal to obtain comparable rostral/caudal levels. We collected 4 sections per animal at -4.0 mm bregma for DH and -5.5 mm bregma for DH, respectively (indicated on **Figure S3c**). Each individual image was analyzed separately using the measurement function in Fiji at the thickest point of the respective pyramidal layer (bilateral analysis, 4*2=8 per animal, averaged). We performed the analysis at three different points along the pyramidal layers that were easy to identify for consistency.

Reverse transcription polymerase chain reaction (RT-PCR) and quantitative real time PCR (qPCR)

RNA extraction and isolation were performed using the miRNAeasy Mini kit (Qiagen, Cat. No. 217004) and the QIAzol Lysis Reagent (Qiagen, Mat. No. 1023537). Two hundred µm-thick tissue sections were obtained using a cryostat (-20°C, Leica, CM3050S) and punches from the DH (14-18 punches per animal), VH (10-14 punches per animal) and PLC (6-8 punches per animal) were collected and kept in dry ice until the RNA extraction procedure. RNA concentration was measured using NanoDrop One (Thermo Scientific) and was in the range of 190 – 380 ng/µl prior to cDNA synthesis. cDNA synthesis was performed using the iScript™ gDNA Clear cDNA Synthesis Kit (BIO RAD, cat. no. 1725035) and the SimpliAmp Thermal Cycler (applied biosystems, Thermo Fisher Scientific) according to the manufacturer protocol. qPCR was conducted using the following 10x QuantiTect primers (diluted in 1.1 mL TE pH 8.0, final concentration: 200nM) purchased from Qiagen: IBA1 (QT01591751), GFAP (QT00195517), IL-1β (QT00181657), IL-6 (QT00182896), Serping1 (QT01607326), C3 (QT00187159), Tm4sf1 (QT01588034), Sphk1 (QT00182035), TNF-α (QT00182896), Hif-1α (QT01830458), Hif-2α (aka EPAS1, QT00192059), AT1aR (QT00375865) and β-Actin (QT00193473, used as the reference gene). All individual qPCR reactions (brain region, primer and condition) were run in triplicate and then averaged.

Assessment of BBB integrity using FITC10, Rho70 and $AngII_{fluo}$

For the assessment of BBB integrity, we performed intra-carotid infusion of two dextran dyes with different molecular weight (FITCH 10kDa and Rho 70kDa) as well as fluorescently-labeled AngII (3µmol/L, Anaspec, CA). Rats were anesthetized with Ketamine/Xylazine (60/8 mg/mL, respectively) and a non-occluding catheter filled with the fluorescent dyes was inserted into the left internal carotid artery as previously described[31]. We used both dyes at 10mg/mL, 2.86µl/g each, with an injection volume of 1mL per rat. We infused the dyes using 0.9% saline and dyes were allowed to circulate for 30 mins. Rats were then decapitated and left in 4% PFA for 48hrs, followed by 30% sucrose for 2-3 days at 4°C. Brains were sectioned using a Cryostat and 40µm-thick sections were mounted for confocal imaging. To detect and quantify the amount of leaked, extravasated FITC 10kDa or $AngII_{fluo}$ we used a digital subtraction approach, in which we subtracted the vessel-bound FITC10 from the total FITC10 (extravascular + intravascular) in Fiji as described before[31].

Losartan treatment

HF rats were randomly allocated two either HF or HF + losartan groups and EF were compared *post hoc* to verify that there were no significant differences in the severity of the myocardial infarction. Losartan-treated rats received losartan (20mg/kg/day) in the drinking water starting 1 week after the HF surgery until they were sacrificed for analysis 13-weeks post-surgery. Weight gain and water consumption was monitored bi-weekly to guarantee adequate consumption of losartan-containing water and comparable food intake between the groups.

Blood Pressure Measurements Using Tail-Cuff Plethysmography

Blood pressure was measured at week 13 prior to sacrifice using the CODA High Throughput Non-Invasive Blood Pressure system (Kent Scientific, Torrington, CT). Experimental settings and recommendations for procedure were based on the work of Daugherty *et al*.[76] Rats were habituated to blood pressure measurements for three consecutive days before experimental recordings were taken and they were acclimated for 10 minutes prior to the start of the measurements. Tail temperatures remained between 32 to 35°C. Blood pressure experimental settings were as follows: occlusion cuffs were inflated to 250 mm Hg and deflated over 20 seconds. The minimum volume changes as sensed by the VPR cuff was set to 15 µL. Each recording session consisted of 25 inflation and deflation cycles with the first five cycles marked as "acclimation" and not considered in the final analysis. At least five valid measurement cycles were obtained for each animal.

Intra-carotid artery infusion for the assessment of blood-brain barrier permeability

Carotid artery infusion was performed as in our previous study[31]. Briefly, with adequate ketamine/xylazine anesthesia (80/20 mg/kg/bw, respectively), rats were placed supine on the surgical table and the neck was shaved. A longitudinal incision was made followed by blunt dissection of omohyoid muscle to expose the underlying right common carotid artery (CCA). The vagus nerve and connective tissue surrounding the CCA were carefully dissected. Using 4-0 silk suture, the caudal end of the CCA was ligated

and a vascular clamp was applied to the rostral end just above the bifurcation of CCA. An incision was made and a PE50 tubing was inserted in a retrograde fashion, and then 4-0 silk suture was used to stabilize the tubing followed by the removal of vascular clamp. All dyes were infused slowly (1 ml over 2 mins) and allowed to circulate for 30 mins before extraction of the brains. Following post-fixation, we acquired confocal images of brain sections containing somatosensory cortex, DH, VH, PVN and CeA and performed binary reconstruction and subtraction of vessel-confined fluorescent signal of confocal images to assess the levels of extravasated dyes in the brain parenchyma, as we previously reported[31].

TUNEL apoptosis staining

TUNEL staining for the identification of apoptotic cells was performed using the Neurotacs™ II In Situ Apoptosis Kit (Trevigen, 4823-30-K) according to the manufacturer's protocol. We used two different approaches (number of apoptotic clusters and area fraction) to measure and quantify the degree of hippocampal cell death (**Extended Fig. 3a, b**). The number of apoptotic clusters were counted manually using the cell count function in Fiji. Area fraction was assessed using the thresholding function as described in Extended Fig. 3a, b.

Acute slice patch clamp electrophysiology

On the day of the experiment, Sham and HF rats were anesthetized with pentobarbital (50 mg/kg^{-1} i.p.) and then perfused transcardially with 40 mL of ice cold aCSF solution with NaCl replaced by equal-osmol sucrose. This sucrose aCSF solution contained (in mM): 200 sucrose, 2.5 KCl, 1 $MgSO_4$, 26 $NaHCO_3$, 1.25 NaH_2PO_4, 20 D-Glucose, 0.4 ascorbic acid, and 2.0 $CaCl_2$; pH 7.2; 300-305 mosmol l^{-1}. The animal was then rapidly decapitated and the brain was subsequently removed for horizontal slicing. The brain was sliced in half longitudinally and a single hemisphere was cut and mounted dorsal side down in the chamber of a vibratome (Leica VT1200s, Leica Microsystems, Buffalo Grove, IL, USA) in accordance with the protocol outlined in Bischofberger et al., 2006. The brain was submerged in sucrose solution and bubbled constantly with 95% O_2/5% CO_2. Horizontal slices were cut at 250 µm thickness and placed in a holding chamber containing aCSF bubbled with 95% O_2/5% CO_2. The aCSF is identical in composition to the sucrose solution, but the 200mM sucrose was replaced with 119 mM NaCl. The slice chamber was warmed using a water bath at 32°C for 20 mins before placement at room temperature for at least 40 mins.

Horizontal slices containing the dorsal hippocampus (CA1) were placed into a specimen chamber on the stage of a Nikon Eclipse FN1 microscope and perfused constantly (~3 ml/min) with aCSF bubbled continuously with 95% O_2/5% CO_2 and warmed to 32°C. CA1 neurons were visualized using the Dragonfly 200 laser spinning disk confocal imaging system and an iXon 888 EMCCD camera (Andor Technology, Belfast, UK). Whole-cell current clamp recordings were obtained from CA1 pyramidal neurons using pipettes (4-5 MΩ) pulled from borosilicate glass (o.d. 1.5 mm) using a P-97 flaming/brown horizontal micropipette puller (Sutter Instruments, Novato, CA). The pipette internal solution consisted of (in mM): 135 $KMeSO_4$, 8 NaCl, 10 HEPES, 2 Mg-ATP, 0.3 Na-GTP, 6 phosphocreatine, 0.2 EGTA with pH 7.2-7.3 and 285-295

mOsmol (kg H_2O)$^{-1}$. The liquid junction potential for the $KMeSO_4$ internal was approximately -10 mV and was not corrected. Recordings were obtained with an Axopatch 200B amplifier (Axon Instruments, Foster City, CA) and digitized using an Axon 1440B Digitizer (Axon Instruments, Foster City, CA) at 10 kHz on a Dell desktop computer running Clampex 10 software (Molecular Devices). CA1 neurons were identified by their anatomical location in the pyramidal laminar layer. Data were discarded if series resistance exceeded a 20% change over the course of the recording. All data are the average of at least two traces in current clamp. Holding current was used to maintain a resting membrane potential of -60mV throughout the recording and there was no correction for liquid junction potential. Data from I-V curves: I-V curves were generated from square pulses of -70pA to +40pA current injections in 10 pA increments, each lasting 1 sec. The steady-state voltage potential was measured at each level and plotted as a function of the amount of current injected. Input resistance: calculated as the slope of the individual I-V curve in each cell. Input/Output curves were generated from square pulses of 0pA to +100pA current injections in 10 pA increments, each lasting 1 sec. The spike frequency and count were measured at each level and plotted as a function of the amount of current injected.

Behavioral studies

Spontaneous Alternation

Spontaneous alternation (SA) is a behavioral task that assesses spatial working memory[77]. Rats have a natural preference to visit environments that they have not been to recently. The assumption underlying SA is that rats must remember their visits to previous locations in order to alternate successfully between spatial locations, which is supported by findings showing that alternation scores are impaired by removing extramaze cues or by increasing the interval between arm choices[77].All testing was conducted during the light phase between 9:00 am and 12:00 pm and the apparatus was cleaned with 70% ethanol after each rat was tested. Each rat was placed in a Y-maze composed of three equally spaced arms (120°; 61 cm x 16.5 cm) and three extra-maze cues were placed on each wall of the testing room and allowed to explore the maze for 8 mins. while an experimenter blind to experimental conditions recorded the sequence and number of arm entries. An alternation was defined as entering three different arms consecutively and a percent alternation score was calculated by dividing the the number of alternations each rat made by the total number of arm entries minus two (i.e., number of alternations possible) and multiplying the resulting quotient by 100.

Inhibitory Avoidance

Three days after SA testing, rats were trained in the one-trial IA task, which assesses emotional, long-term memory[78]. All testing was conducted during the light phase between 9:00 am and 12:00 pm and the apparatus was cleaned with 70% ethanol after each rat was tested. For both training and testing, rats were placed in a polycarbonate trough-shaped apparatus (84 x 20 cm x 34 cm) that was divided into a lighted (24 cm) and dark compartment (60 cm) by a retractable polycarbonate guillotine door. The dark compartment had a metal floor through which shock could be delivered. The lighted compartment was

illuminated by a 60 W lamp and was the only light source in the room. For training, a rat was placed in the lighted side of the apparatus facing away from the door and the door was lowered when it turned around or after 12 sec passed. As soon as the rat entered the dark compartment with all four paws, the door was closed and a 0.5 mA/1 sec footshock (Coulbourn) was administered, and then the rats was removed from the apparatus 5 sed later. The current level was verified using a digital multimeter (AstroAI AM33D) before, during, and after the experiment. The latency to enter the dark compartment was recorded. The retention test was conducted 24hrs later using the same procedure, with the exception that footshock was not administered. Latency to enter the dark compartment (maximum 600 sec) was recorded and used as an index of the retention of the training, with longer latencies indicative of better memory.

Statistical analyses

All statistical analyses were performed using GraphPad Prism 9 (GraphPad Software, California, USA). Student's t-test, one- or two-way analysis of variance (ANOVA) were used to compare the groups followed by Tukey post-hoc tests. Results are expressed as mean ± standard error of the mean (SEM). Results were considered statistically significant if $p<0.05$ and are presented as * for $p<0.05$, ** for $p<0.01$ and *** for $p<0.0001$ in the respective Figures.

Funding

This work was supported by DFG Postdoc Fellowship AL 2466/1-1 to FA; National Heart, Lung, and Blood Institute Grant NIH HL090948 to JES, National Institute of Neurological Disorders and Stroke Grant NIH NS094640 to JES, and funding provided by the Center for Neuroinflammation and Cardiometabolic Diseases (CNCD) at Georgia State University.

Acknowledgements

The authors cordially thank Marina Eliava (Central Institute of Mental Health, Mannheim) for the scientific illustrations on Figure 2 and Figure 10. We thank Elliot Albers and Kim Huhman (Neuroscience Institute, Georgia State University) for allowing us to use their cryostats. The authors also thank Atit Patel and Daniel Cox (Neuroscience Institute, Georgia State University) for assistance with the qPCR analysis. We thank Eric G. Krause and Justin Smith (Department of Pharmacodynamics, College of Pharmacy, University of Florida) for helping us to troubleshoot the RNAScope assay.

Figures

Figure 1

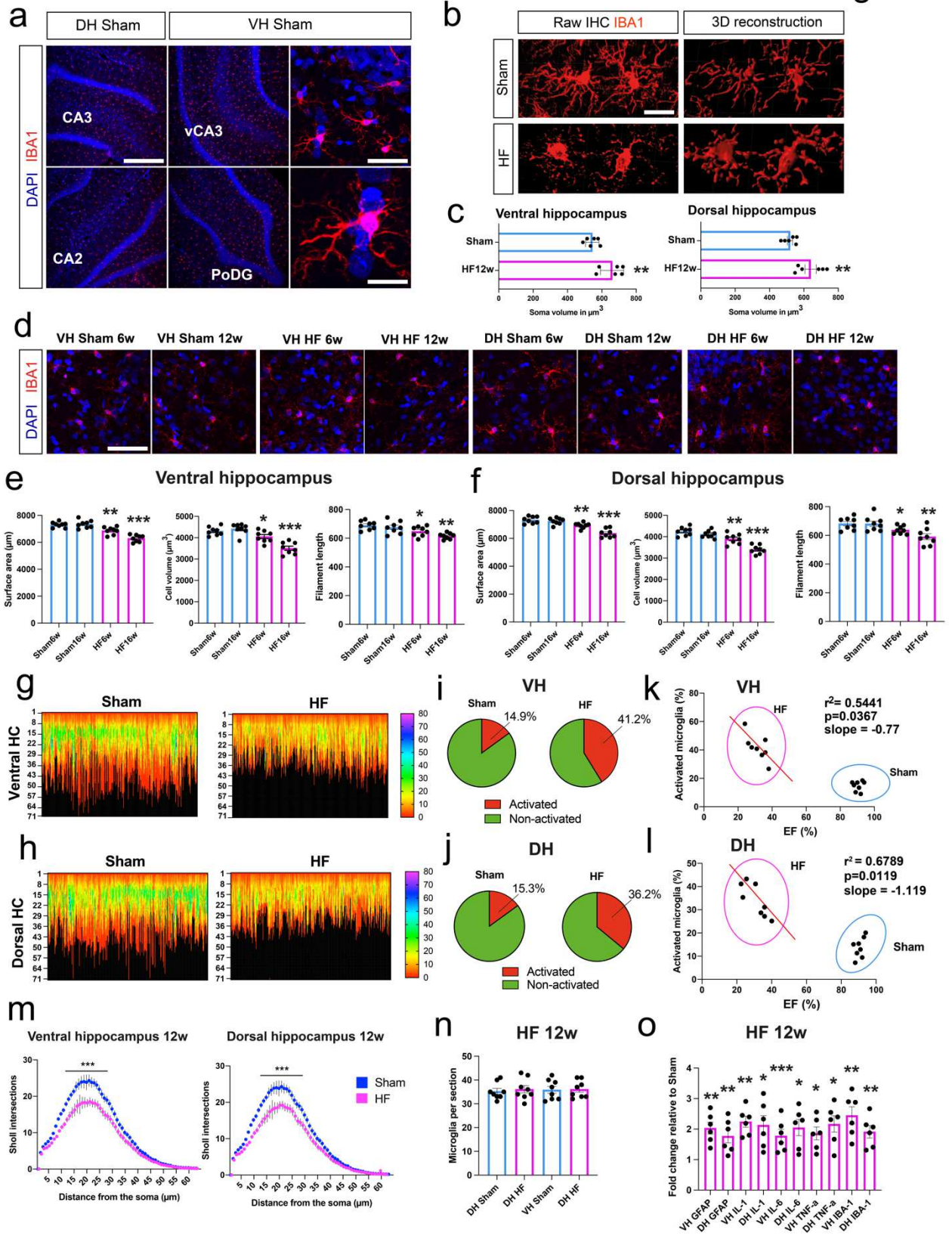

Figure 1 Microglial activation and increased cytokine levels in the hippocampus of HF rats
a Confocal images showing IBA1-positive microglia in the DH and VH of sham rats. (v)CA2/3 = (ventral) cornu ammonis 2/3, PoDG = polymorph layer of dentate gyrus. **b** Images of microglia and their three-dimensional reconstruction in sham and HF rats; **c** Three-dimensional assessment of somatic volume (n=6 per group). **d** Representative confocal images depicting microglial morphology at two different timepoints. **e, f** Quantification of various microglial morphology parameters following three-dimensional reconstruction. HF rats displayed a de-ramified microglial phenotype with reduced cell volume, surface area and filament length (n=8 per group). **g, h** Heat map analysis (256 microglia, 32 per animal, 8 rats per group) of microglial morphology reveals a less complex and reduced domain size in HF rats. Left numbers indicate microglial reach (in µm), color coding indicates peak Sholl values of individual microglia. **i, j** The percentage of activated microglia (Peak sholl value<10) is higher in HF rats. **k, l** The percentage of activated microglia correlates with the severity of disease (EF%) in HF rats. Pink circles represent HF rats, blue circles represent sham rats (n=8 per group). **m** Sholl analysis for microglia in sham and HF rats. **n** Microglial cell counting revealed no difference between sham and HF animals (n=8 rats per group). **o** Quantification of cytokine mRNA levels via qPCR (n=6 per group). $p<0.05$*, $p<0.01$** and $p<0.001$***. Scale bars 300µm (a), 25µm (a), 10µm (a), 10µm (b) and 50µm (c).

Figure 2

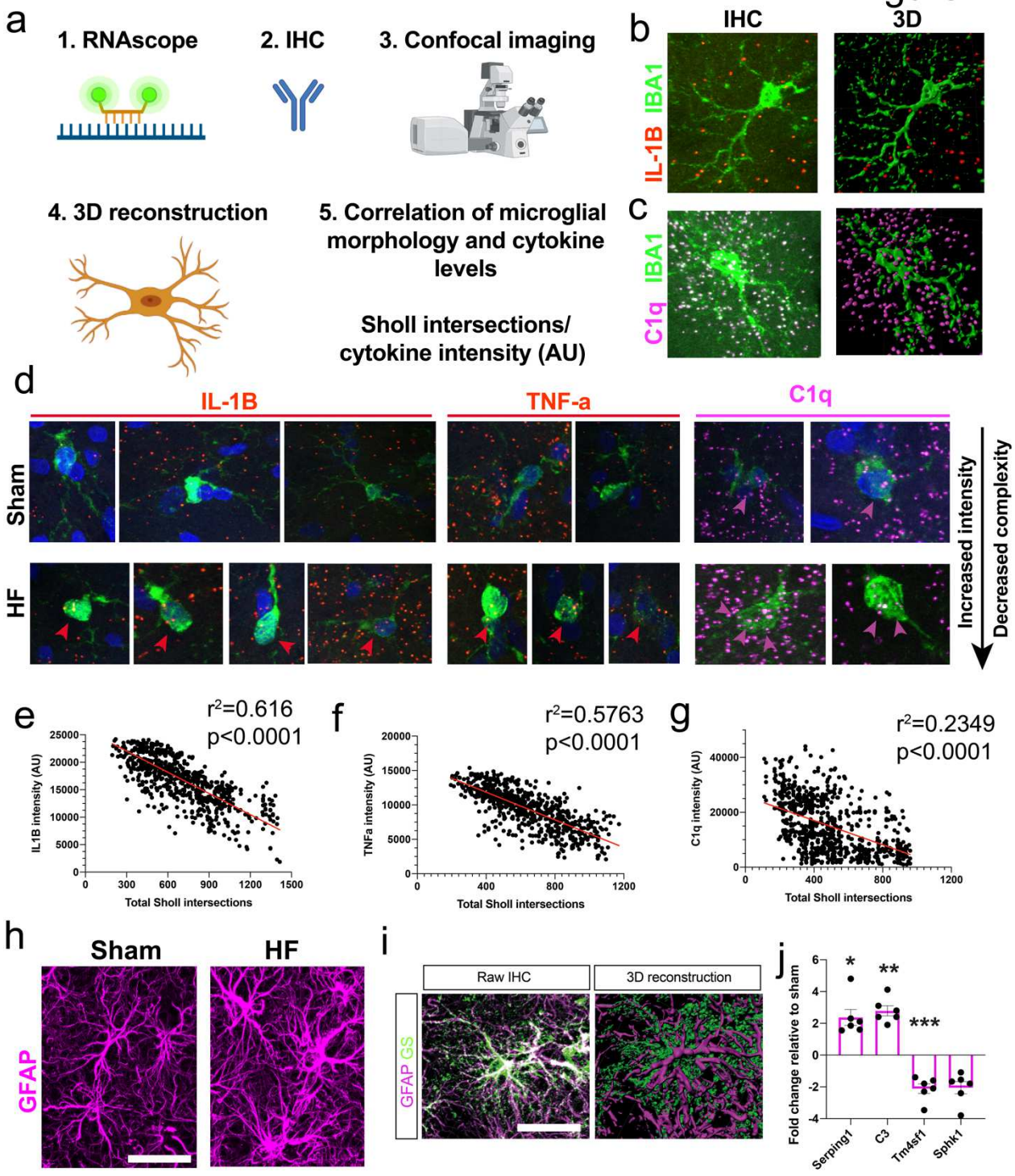
a
1. RNAscope
2. IHC
3. Confocal imaging
4. 3D reconstruction
5. Correlation of microglial morphology and cytokine levels
Sholl intersections/ cytokine intensity (AU)
b
IHC
3D
IBA1
IL-1B
c
IBA1
C1q
d
IL-1B
TNF-a
C1q
Sham
HF
Increased intensity
Decreased complexity
e
r²=0.616
p<0.0001
IL1B intensity (AU)
Total Sholl intersections
f
r²=0.5763
p<0.0001
TNFa intensity (AU)
Total Sholl intersections
g
r²=0.2349
p<0.0001
C1q intensity (AU)
Total Sholl intersections
h
Sham
HF
GFAP
i
Raw IHC
3D reconstruction
GFAP GS
j
Fold change relative to sham
Serping1
C3
Tm4sf1
Sphk1

Figure 2 Cytokine transcripts correlate with microglial morphology and predict astrocyte complexity in HF

a Schematic depiction of workflow for *in situ* hybridization, reconstruction of microglial morphology and correlation of microglial complexity with cytokine mRNA levels**. b, c** Representative images showing raw and three-dimensional reconstructions of microglia of a sham rat negative for IL-1β (b) and positive for C1q (c). **d** Representative images of IL1β, TNF-α or C1q mRNA in microglia in sham and HF rats. Note that less complex microglia in HF rats (bottom rows) have more cytokine mRNA. Arrowheads indicate co-localization of IBA1 fluorescence and cytokine mRNA probe visualized via RNAScope. **e, f, g** The amount of cytokine mRNA is negatively correlated with microglial complexity (measured by the total number of sholl intersections, each dot represents a single microglia, plot is a pool of microglia obtained from n=4 rats per group). **h** Typical images of normal and hypertrophic astrocytes in sham and HF rats respectively. **i** Example of a three-dimensionally reconstructed astrocyte via GFAP and GS. **j** Quantification of A1/A2 astrocyte markers via qPCR in sham and HF rats (n=6 per group). $p<0.05$*, $p<0.01$** and $p<0.001$***. GFAP = glial fibrillary acidic protein; GS = glutamine synthetase. Scale bars 75μm (a), 10μm (b) and 20μm (h).

Figure 3

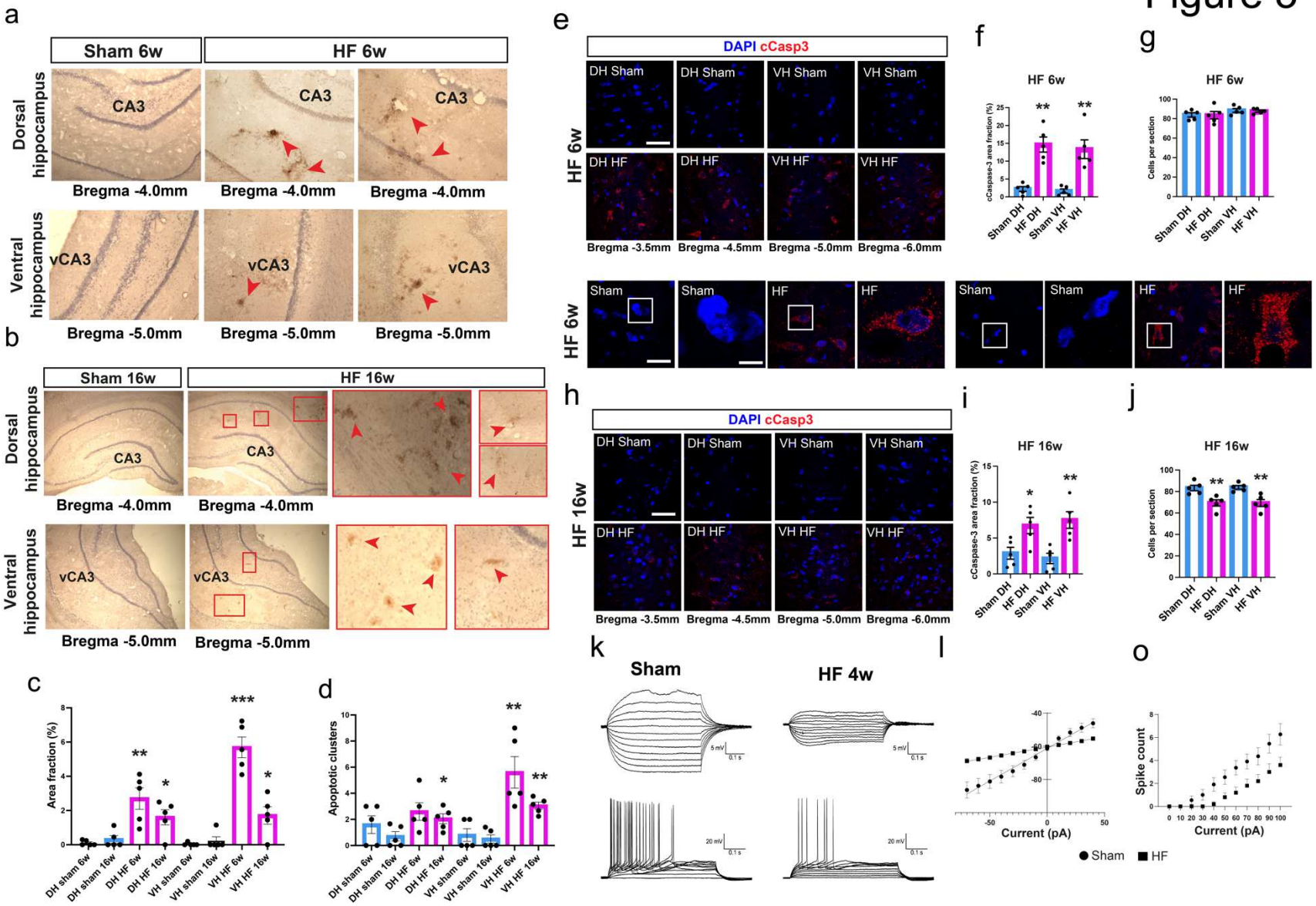
a
Sham 6w
HF 6w
Dorsal hippocampus
CA3
Bregma -4.0mm
Ventral hippocampus
vCA3
Bregma -5.0mm
b
Sham 16w
HF 16w
c
Area fraction (%)
DH sham 6w
DH sham 16w
DH HF 6w
DH HF 16w
VH sham 6w
VH sham 16w
VH HF 6w
VH HF 16w
d
Apoptotic clusters
e
DAPI cCasp3
DH Sham
VH Sham
DH HF
VH HF
HF 6w
Bregma -3.5mm
Bregma -4.5mm
Bregma -5.0mm
Bregma -6.0mm
Sham
HF
f
HF 6w
cCaspase-3 area fraction (%)
Sham DH
HF DH
Sham VH
HF VH
g
HF 6w
Cells per section
h
DAPI cCasp3
HF 16w
i
HF 16w
cCaspase-3 area fraction (%)
j
HF 16w
Cells per section
k
Sham
HF 4w
l
Current (pA)
Sham
HF
o
Spike count
Current (pA)

Figure 3 Early onset of heart failure-induced apoptosis and altered neuronal function

a, b Images show TUNEL-based detection of apoptotic clusters (arrowheads) in DH and VH of HF rats at 6- and 16-weeks post-surgery (n=5 per group); (v)CA3 = (ventral) cornu ammonis 3. **c, d** Quantification of area fraction and number of apoptotic clusters in sham and HF rats. **e** Images of cCasp3-positive cells at 6-weeks post HF surgery (n=5 per group). Note the absence of cCasp3 staining in sham rats. **f, g** Quantification of cCasp3-positive immunoreactivity and cell numbers in DH and VH of sham and HF rats at 6-weeks post-surgery (n=5 per group). Note that the number of DAPI-positive cells is not reduced in HF animals 6 weeks post-surgery. **h** Images of cCasp3-positive cells at 16-weeks post HF surgery (n=5 per group). Note the absence of cCasp3 staining in sham rats and the weaker cCasp3 staining compared to HF 6w rats. **i, j** Quantification of cCasp3-positive immunoreactivity and cell numbers in DH and VH of sham and HF rats at 6-weeks post-surgery (n=5 per group). Note that the number of DAPI-positive cells is reduced in HF animals 16 weeks post-surgery. **k** I-V curves (top) and positive ramping current injections (bottom) from CA1 pyramidal neurons of Sham (left) and HF (right) rats. Note the decreased input resistance and increased rheobase of HF neurons relative to sham. **l** I-V curve summary of sham (circles) and HF (squares). (sham n= 2 animals/ 11 cells; HF n= 3 animals/9 cells) **o** Input/output calculations measured as number of spikes evoked as a function of current injected as a 500 ms pulse (sham n= 2 animals/ 11 cells; HF n= 3 animals/9 cells). $p<0.05$*, $p<0.01$** and $p<0.001$***. Scale bars 100µm (e), 50µm (e) and 100µm (f).

Figure 4

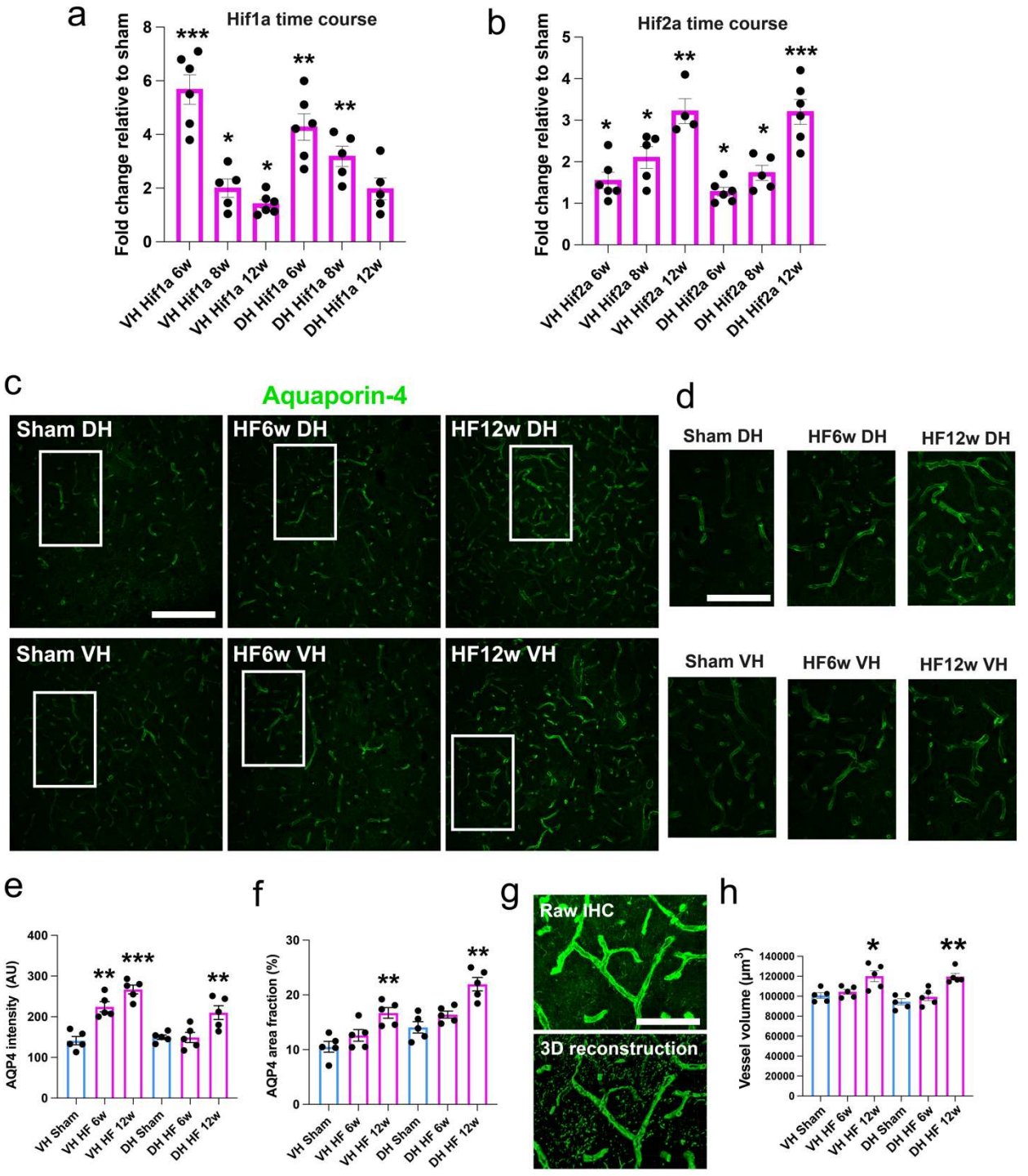
a
Hif1a time course
Fold change relative to sham
VH Hif1a 6w
VH Hif1a 8w
VH Hif1a 12w
DH Hif1a 6w
DH Hif1a 8w
DH Hif1a 12w
b
Hif2a time course
Fold change relative to sham
VH Hif2a 6w
VH Hif2a 8w
VH Hif2a 12w
DH Hif2a 6w
DH Hif2a 8w
DH Hif2a 12w
c
Aquaporin-4
Sham DH
HF6w DH
HF12w DH
Sham VH
HF6w VH
HF12w VH
d
Sham DH
HF6w DH
HF12w DH
Sham VH
HF6w VH
HF12w VH
e
AQP4 intensity (AU)
VH Sham
VH HF 6w
VH HF 12w
DH Sham
DH HF 6w
DH HF 12w
f
AQP4 area fraction (%)
VH Sham
VH HF 6w
VH HF 12w
DH Sham
DH HF 6w
DH HF 12w
g
Raw IHC
3D reconstruction
h
Vessel volume (μm3)
VH Sham
VH HF 6w
VH HF 12w
DH Sham
DH HF 6w
DH HF 12w

Figure 4 Hypoxia and pathological angiogenesis in the hippocampus of HF rats

a, b qPCR assessment of changes in hypoxia markers Hif-1α and Hif-2α mRNA 6, 8- and 12-weeks post-surgery (n=5 per group). **c, d** Representative images in sham and HF rats showing vascularization (Aquaporin 4 (AQP4) immunoreactivity) of VH and DH at 6- and 12- weeks post-surgery. **e, f** Quantification of AQP4 signal intensity and area fraction volume in sham and HF rats (n=5 per group). **g** Three-dimensional reconstruction of vessel volume using AQP4 fluorescence. **h** Quantification of vessel volume by three-dimensional reconstruction (n=5 per group). $p<0.05$*, $p<0.01$** and $p<0.001$***. Scale bars 100µm (c), 25µm (d) and 25µm (g).

Figure 5

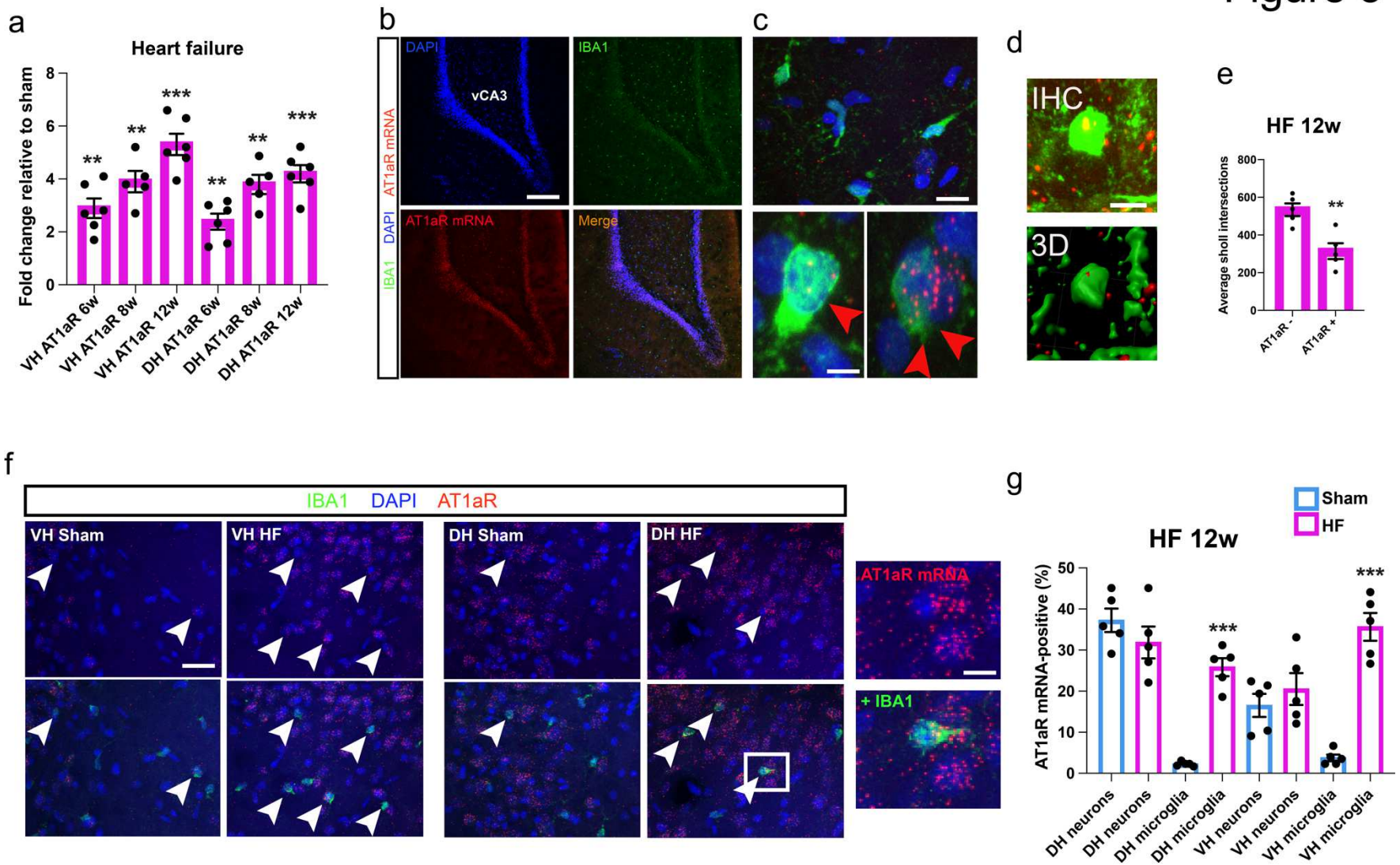
a
Heart failure
Fold change relative to sham
VH AT1aR 6w
VH AT1aR 8w
VH AT1aR 12w
DH AT1aR 6w
DH AT1aR 8w
DH AT1aR 12w
b
DAPI
IBA1
vCA3
AT1aR mRNA
Merge
c
d
IHC
3D
e
HF 12w
Average sholl intersections
AT1aR -
AT1aR +
f
IBA1 DAPI AT1aR
VH Sham
VH HF
DH Sham
DH HF
AT1aR mRNA
+ IBA1
g
Sham
HF
HF 12w
AT1aR mRNA-positive (%)
DH neurons
DH neurons
DH microglia
DH microglia
VH neurons
VH neurons
VH microglia
VH microglia

Figure 5 Microglia-specific AT1a receptor (AT1aR) upregulation in HF rats

a Time course of changes in AT1a mRNA levels in HF rats at 6-, 8- and 12-weeks post-surgery (n=5/6 per group). **b** Confocal images showing AT1aR mRNA in situ combined with IHC against IBA1 in the VH of sham rats; vCA3 = ventral cornu ammonis 3. **c** High magnification confocal images show co-localization of AT1aR mRNA with IBA1-labeled microglia in a sample from a HF rat. Arrowheads indicate weak and strong AT1aR colocalization in IBA1-positive microglia. **d** Three-dimensional reconstruction confirms the presence of AT1aR mRNA in activated microglia of HF rats. **e** AT1aR-positive microglia are less complex than AT1aR-negative microglia (n=5 per group). **f** Representative confocal images of AT1aR-positive microglia in DH and VH of sham and HF rats. White arrowheads indicate colocalization of IBA1 immunoreactivity and AT1aR mRNA. **g** AT1aR mRNA is significantly increased in DH and VH microglia, but not neurons identified by their location within the pyramidal cell layers, of HF rats. $p<0.05$*, $p<0.01$** and $p<0.001$***. Scale bars 250μm (a), 20μm (b), 5μm (b), 10μm (c), 25μm (e), 5μm (f) and 10μm (f).

Figure 6

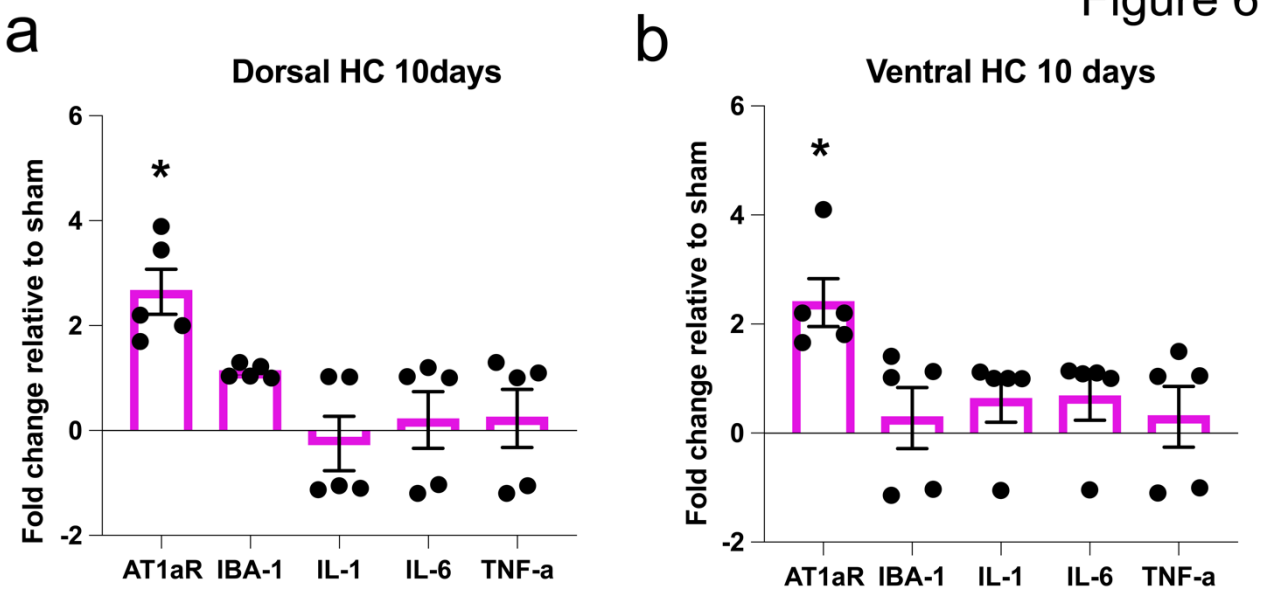

Figure 6 Hypoxia and elevated AT1aR levels precede cytokine increase in HF rats
a, b qPCR assessment of Hif1α, Hif2α, AT1aR, IB1, IL1β, IL6 and TNFα mRNA levels in the DH and VH of HF rats 10 days post HF surgery (n=5 per group).

Figure 7

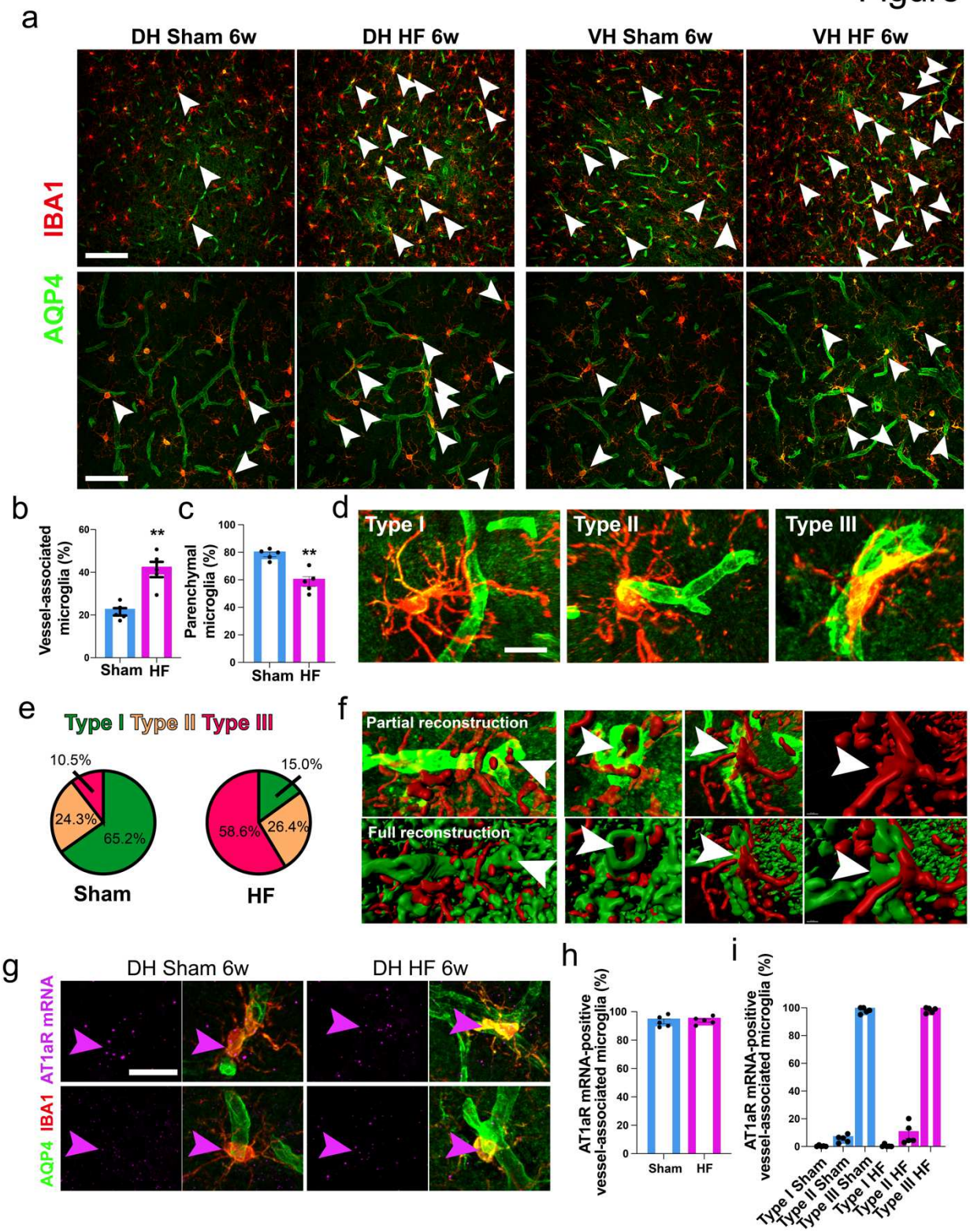
a
DH Sham 6w
DH HF 6w
VH Sham 6w
VH HF 6w
IBA1
AQP4
b
Vessel-associated microglia (%)
Sham
HF
c
Parenchymal microglia (%)
Sham
HF
d
Type I
Type II
Type III
e
Type I Type II Type III
10.5%
24.3%
65.2%
Sham
15.0%
58.6%
26.4%
HF
f
Partial reconstruction
Full reconstruction
g
DH Sham 6w
DH HF 6w
AT1aR mRNA
IBA1
AQP4
h
AT1aR mRNA-positive vessel-associated microglia (%)
Sham
HF
i
AT1aR mRNA-positive vessel-associated microglia (%)
Type I Sham
Type II Sham
Type III Sham
Type I HF
Type II HF
Type III HF

Figure 7 Increased number of AT1aR-positive, AQP4-associated microglia in HF rats
a Confocal images showing IBA1-positive microglia and AQP4-labeled blood vessels in sham and HF rats. Arrowheads point to vessel-associated microglia **b, c** Quantification of vessel-associated and parenchymal microglia (n=5 per group). **d** Classification of Type I-III vessel-associated microglia. **e** Pie charts showing the relative incidence of Type I-III microglia in sham and HF rats (n=5 per group). **f** Three-dimensional reconstruction highlights vessel-protruding microglial filaments in HF rats. Arrowheads indicate IBA1-positive filaments within AQP4-labeled vessel lumen. **g** Images showing samples of AT1aR mRNA expression (arrowheads) in vessel-associated microglia. **h** Quantification showing that the vast majority of vessel-associated microglia are positive for AT1aR mRNA both in sham and HF rats (n=5 per group). **i** Quantification of vessel-associated microglia reveals that the majority of AT1aR-positive microglia are Type III vessel-associated microglia (n=5 per group). $p<0.05$*, $p<0.01$** and $p<0.001$***. Scale bars 150µm (a), 75µm (a), 10µm (d) and 10µm (g).

Figure 8

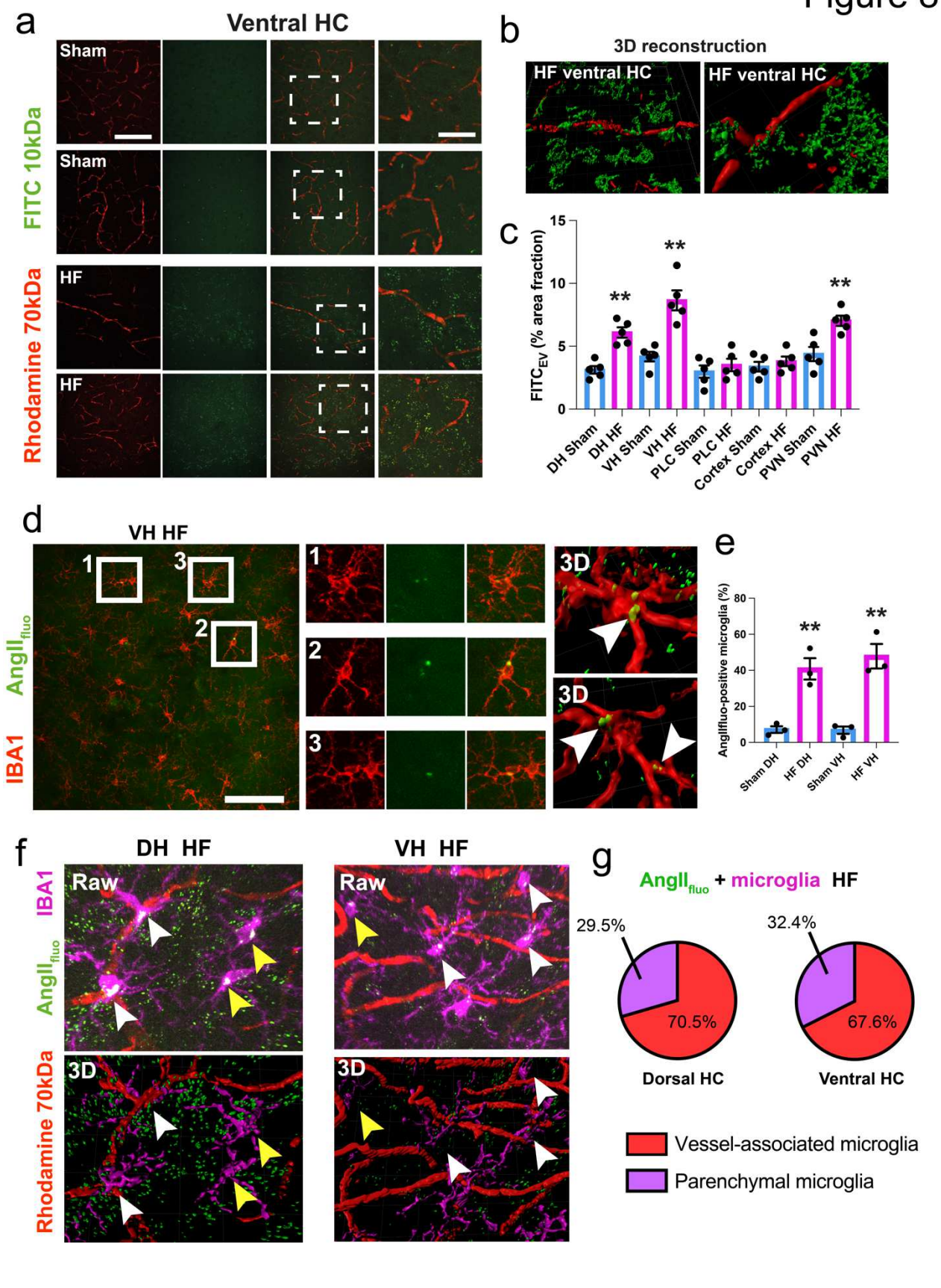
a
Ventral HC
Sham
Sham
HF
HF
FITC 10kDa
Rhodamine 70kDa
b
3D reconstruction
HF ventral HC
HF ventral HC
c
FITC_EV (% area fraction)
DH Sham
DH HF
VH Sham
VH HF
PLC Sham
PLC HF
Cortex Sham
Cortex HF
PVN Sham
PVN HF
d
VH HF
AngII_fluo
IBA1
3D
3D
e
Angiffluo-positive microglia (%)
Sham DH
HF DH
Sham VH
HF VH
f
DH HF
VH HF
Raw
Raw
IBA1
AngII_fluo
Rhodamine 70kDa
3D
3D
g
AngII_fluo + microglia HF
29.5%
70.5%
32.4%
67.6%
Dorsal HC
Ventral HC
Vessel-associated microglia
Parenchymal microglia

Figure 8 Compromised BBB and uptake of circulating AngII by microglia in HF rats
a Confocal images showing rhodamine 70 (red) and FITC10 (green) staining in the VH of a sham and HF rats following their systemic infusion. Note the increased extravasated FITC10 (green) in the HF rat. **b** Three-dimensional reconstruction of blood vessels (intravascularly stained with Rho70, red) reveals perivascular clustering of FITC10 (green), as well as what appears to be accumulation of the dye in neuronal profiles in close proximity to the blood vessels. **c** Quantification of extravasated FITC10 ($FITC_{EV}$) in the DH, VH, somatosensory cortex, PLC and PVN of sham and HF rats (n=5 per group). **d** Confocal images show parenchymal leakage of fluorescently-labeled $AngII_{flu}$ (green) in the VH of a HF rat. Insets 1-3 (corresponding to the squared areas in left panel) show clear co-localization of $AngII_{fluo}$ with IBA1-positive microglia. Three-dimensional reconstructions (right panels) shows that $AngII_{fluo}$ is taken up by microglia and accumulates both in processes and somata (indicated by white arrowheads). Microglia have been made transparent for better visibility of $AngII_{fluo}$**. e** Quantification of $AngII_{fluo}$-positive microglia in DH and VH in sham and HF rats (n=3 per group). **f** Sample images of co-infusion of Rho70 and $AngII_{fluo}$ to discriminate between $AngII_{fluo}$-positive, vessel-associated and parenchymal microglia in DH and VH of a HF rat. White arrowheads indicate co-localization of $AngII_{fluo}$ and IBA1-positive vessel-associated microglia, yellow arrowheads indicate $AngII_{fluo}$ bound to parenchymal microglia. Three-dimensional reconstructions show clear overlap of IBA1 and $AngII_{fluo}$. **g** Pie charts show the proportion of $AngII_{fluo}$-positive, vessel-associated microglia in DH and VH of HF rats (n=2 per group) 2-weeks post-surgery. $p<0.05$*, $p<0.01$** and $p<0.001$***. Scale bars 150 µm (a), 50 µm (a), 100 µm (d) and 10 µm (f).

Figure 9

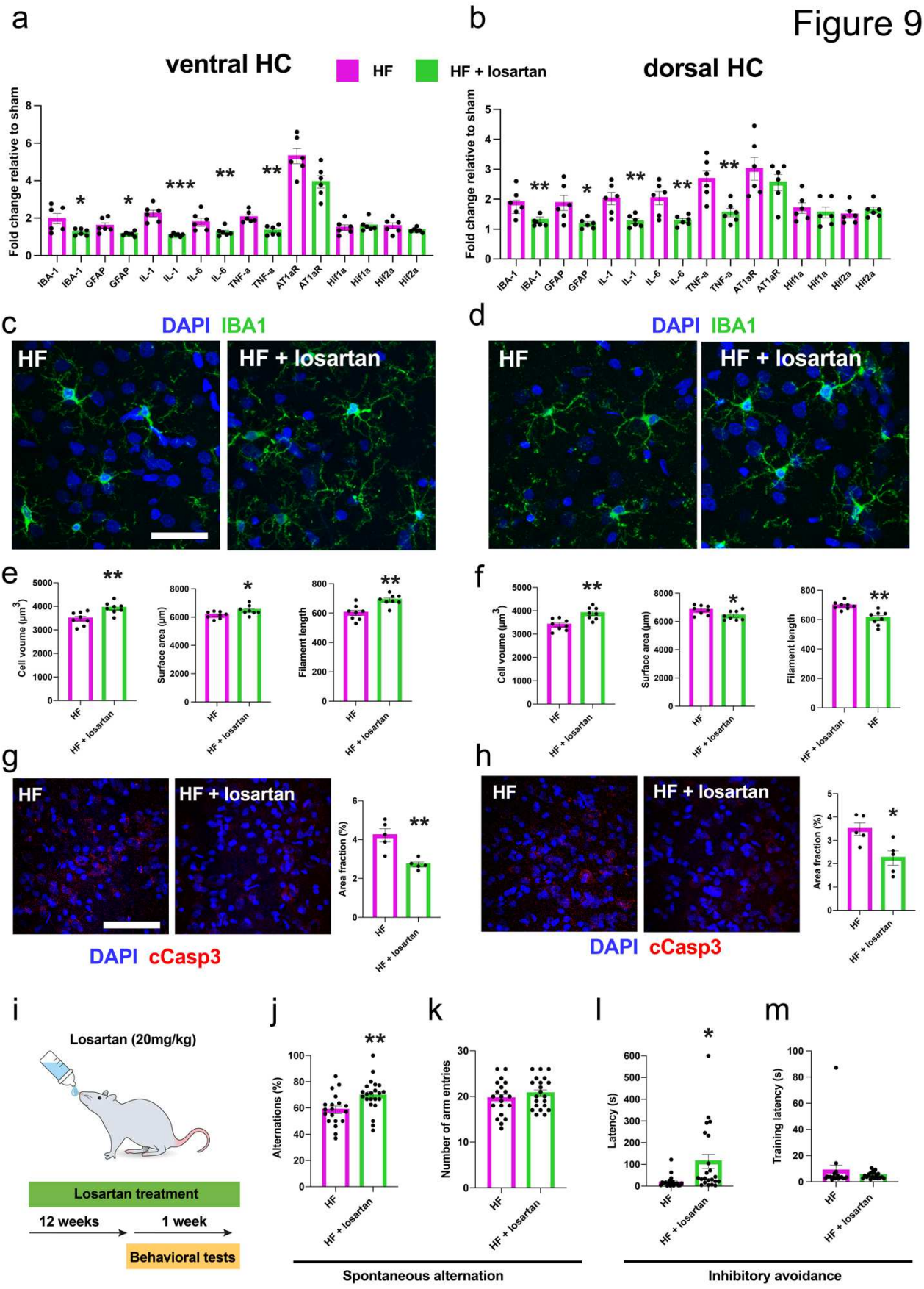

1148

Figure 9 AT1aR blockade improves neuroinflammation and improves cognitive performance in HF rats

a, b AT1aR blockade (losartan) reduced mRNA levels of IBA1, GFAP and various cytokines, but not AT1aR, Hif-1α or Hif-2α in HF rats (n=6 per group, 12 weeks post-surgery). **c, d** Representative images of microglia in HF rats with and without losartan treatment. **e, f** Assessment of microglial cell volume, surface area and filament length using three-dimensional reconstruction in HF rats with and without Losartan treatment (n=6 per group, 12 weeks post-surgery). **g, h** Losartan treatment significantly reduced cCasp3 immunoreactivity in VH and DH of HF rats (n=5 per group). **i-m** Effect of losartan treatment on two different behavioral paradigms (n=19 HF, n=22 HF + Losartan). HF rats subjected to losartan treatment displayed significantly more spontaneous alternations (**j**), which are not due to hyperactivity as indicated by similar total number of arm entries in the two groups (**k**). Losartan-treated animals have a higher retention latency during inhibitory avoidance testing (**l**). **m** No difference in training latencies between HF and HF + Losartan rats. $p<0.05$*, $p<0.01$** and $p<0.001$***. Scale bars 25 µm (c) and 150 µm (g).

Figure 10

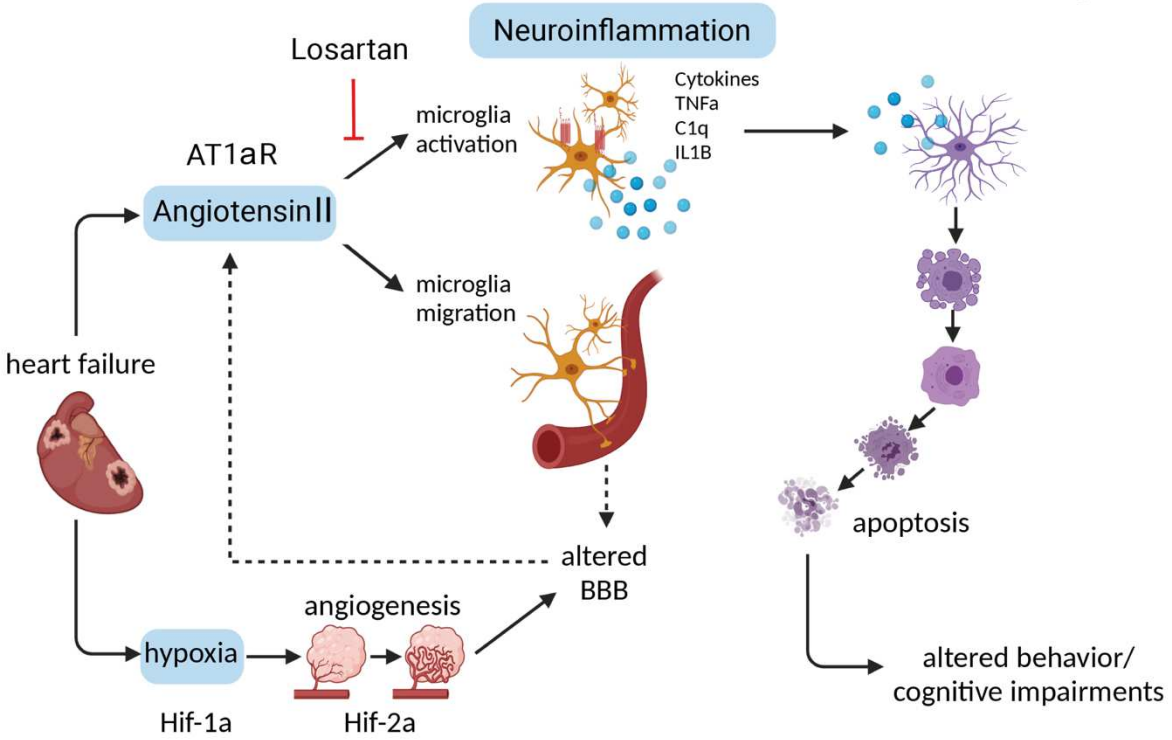

Figure 10 Schematic depicting the proposed mechanism underlying cognitive impairment in HF rats

Figure S1

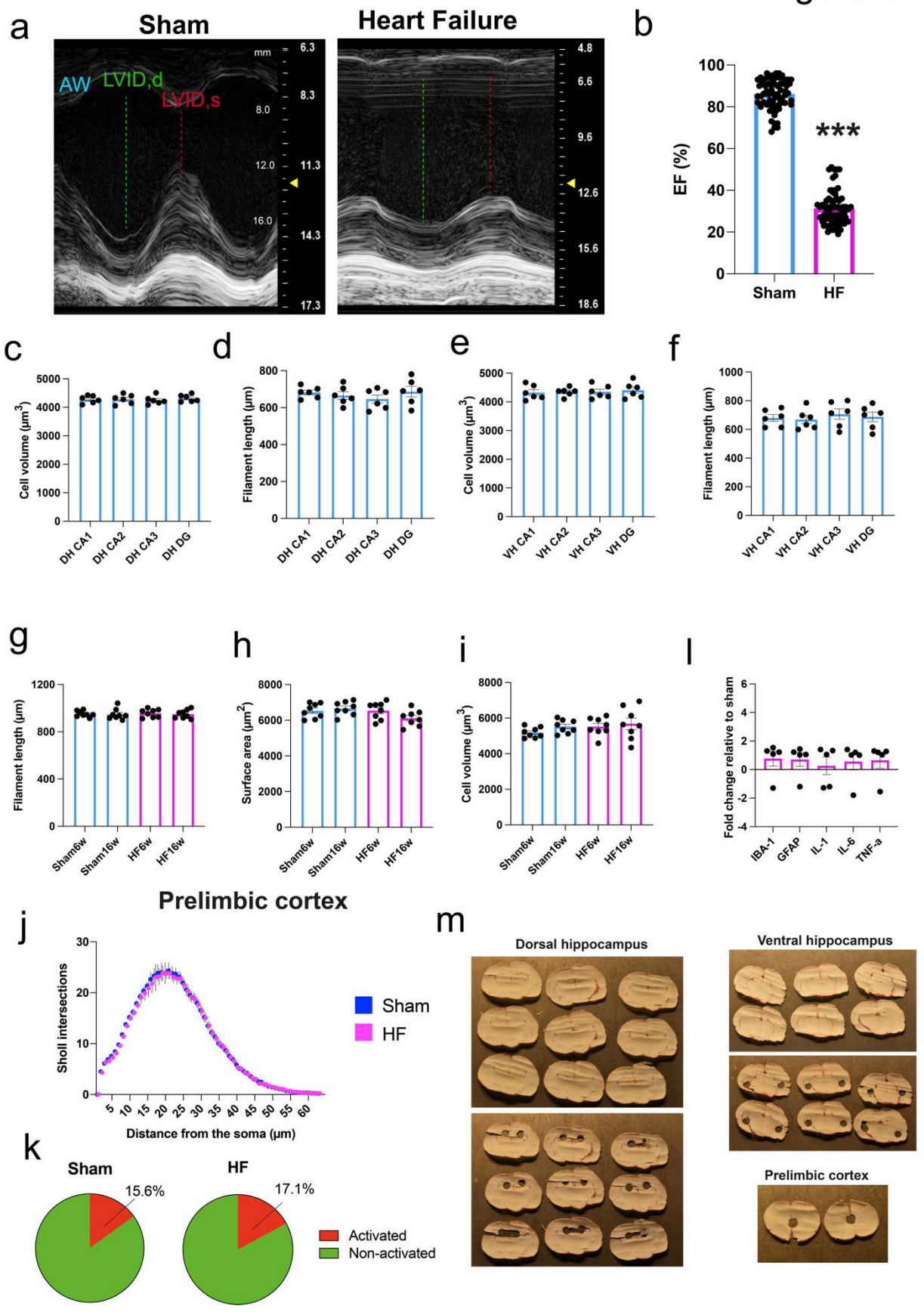
a
Sham
Heart Failure
AW
LVID,d
LVID,s
mm
b
EF (%)
Sham
HF
***
c
Cell volume (µm3)
DH CA1
DH CA2
DH CA3
DH DG
d
Filament length (µm)
e
VH CA1
VH CA2
VH CA3
VH DG
f
g
Sham6w
Sham16w
HF6w
HF16w
h
Surface area (µm2)
i
l
Fold change relative to sham
IBA-1
GFAP
IL-1
IL-6
TNF-a
Prelimbic cortex
j
Sholl intersections
Distance from the soma (µm)
k
15.6%
17.1%
Activated
Non-activated
m
Dorsal hippocampus
Ventral hippocampus
Prelimbic cortex

Figure S1 a Assessment of cardiac ejection fraction in a sham and HF rat using echocardiography. **b** Ejection fraction of all rats used for this study (151 total, n=56 sham, n=95 HF). **c-f** Quantification of microglia volume and filament length via three-dimensional reconstruction reveals no significant differences across various hippocampal subdivisions (n=6 per group). For the sake of simplicity, microglia were pooled and referred to as DH and VH microglia hereafter. **g-i** No difference in prelimbic cortex (PLC) microglial morphology between sham and HF rats (n=6 per group). **j** Sholl analysis reveals no differences in PLC microglial complexity between sham and HF rats. **k** No changes in the number of activated microglia in the PLC of HF rats. **l** Cytokine mRNA levels in the PLC of HF rats does not increase (n=5 per group). **m** Images depict the location of tissue punches obtained from brain sections (100 µm thick) used for the brain region-specific qPCR. $p<0.05$*, $p<0.01$** and $p<0.001$***.

1295

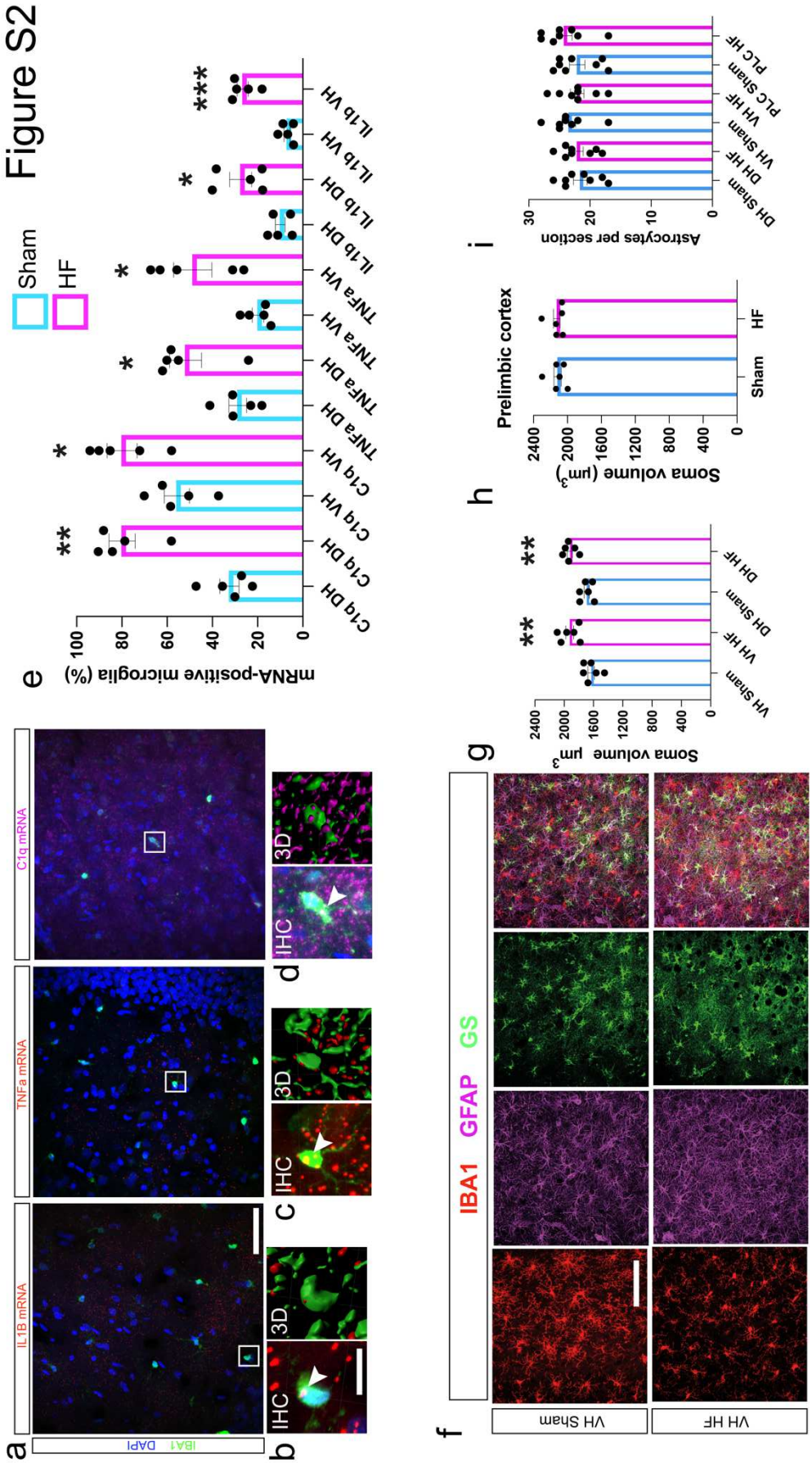
Figure S2
a
IL1B mRNA
TNFa mRNA
C1q mRNA
IBA1 DAPI
b
IHC
3D
c
IHC
3D
d
IHC
3D
e
Sham
HF
mRNA-positive microglia (%)
C1q DH
C1q DH
C1q VH
C1q VH
TNFa DH
TNFa DH
TNFa VH
TNFa VH
IL1b DH
IL1b DH
IL1b VH
IL1b VH
f
IBA1 GFAP GS
VH Sham
VH HF
g
Soma volume µm3
VH Sham
VH HF
DH Sham
DH HF
h
Prelimbic cortex
Soma volume (µm3)
Sham
HF
i
Astrocytes per section
DH Sham
DH HF
VH Sham
VH HF
PLC Sham
PLC HF

Figure S2 a Confocal images of RNAScope in situ hybridization for detection of cytokines IL1β, TNF-α and C1q in combination with IBA1 antibody staining in HF rats. **b, c, d** High magnification images show co-localization of cytokines and IBA1 using three-dimensional reconstruction. White arrowheads indicate co-localization. **e** Quantification of microglia-specific mRNA cytokine levels in DH and VH of sham and HF rats (n=5 per group). **f** Panel shows IBA1-positive microglia and GFAP/GS-labeled astrocytes in sham and HF rats. **g** Assessment of astrocyte soma volume using three-dimensional reconstruction for VH and DH astrocytes (n=6 per group). **h** No difference in astrocyte soma volume in the PLC between sham and HF rats. **i** No difference in astrocyte number were observed between sham and HF rats for VH, DH and PLC (n=8 per group). Scale bars 10 μm (b) and 100 μm (f). $p<0.05$*, $p<0.01$** and $p<0.001$***.

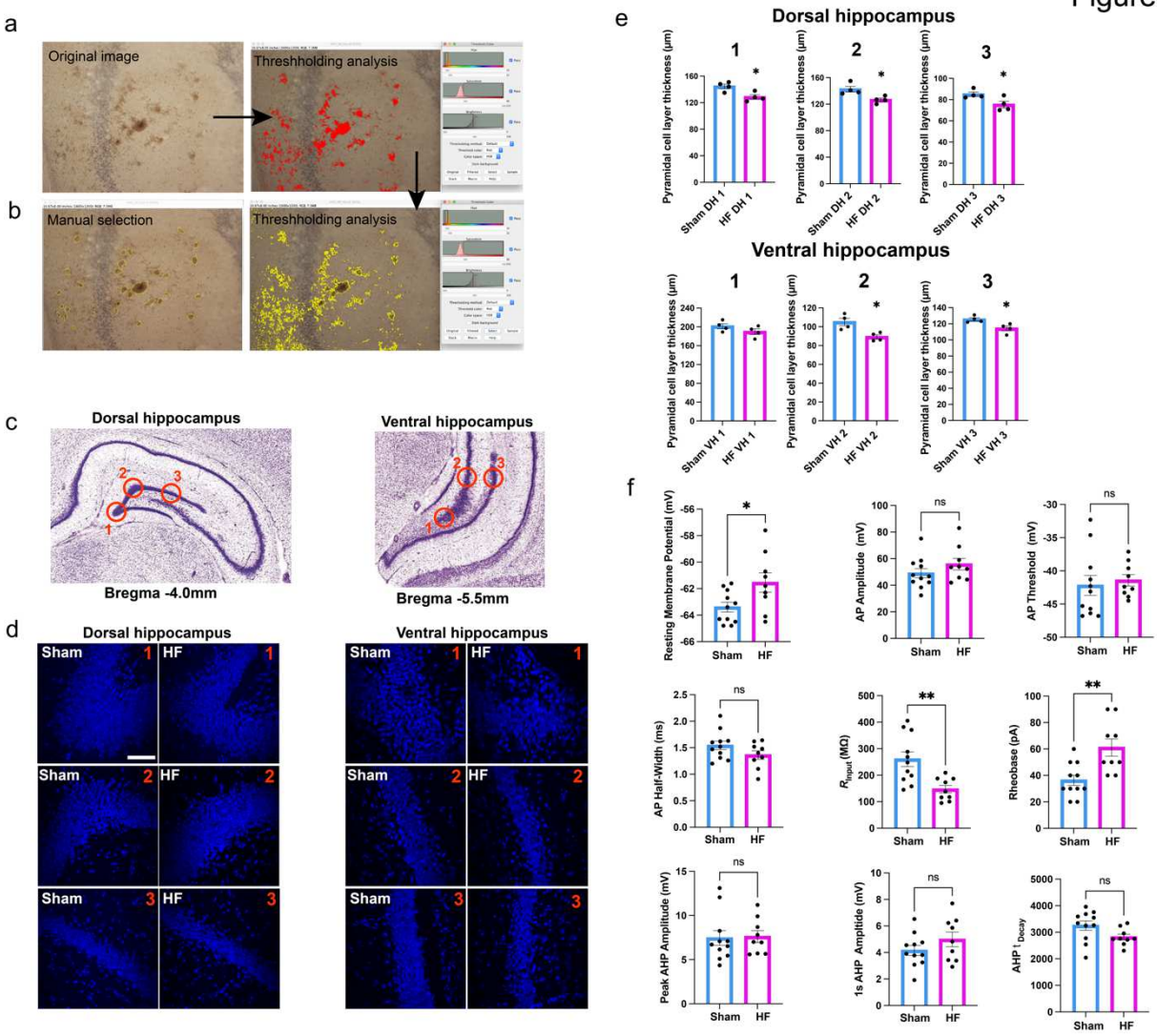

Figure S3 a,b Images show the different steps for thresholding analysis and manual selection of apoptotic clusters using the software Fiji. **c** Pyramidal cell layer landmarks for the detailed analysis of pyramidal cell layer thinning in HF rats. **d** High magnification confocal images depict thinning of pyramidal cell layers in HF rats across multiple different points, as indicated in **c**. **e** Quantification of pyramidal cell layer thickness in DH and VH of sham and HF rats. **f** Summary data of multiple electrophysiological parameters obtained via patch-clamp recordings in CA1 neurons from slices of sham and HF rats. AP: action potential; Rinput: input resistance; AHP: afterhyperpolarization, AHP1s: AHP amplitude measured 1 second after the end of the spike train. Scale bar 75 µm (d). $p<0.05$* and $p<0.01$**.

Figure S4

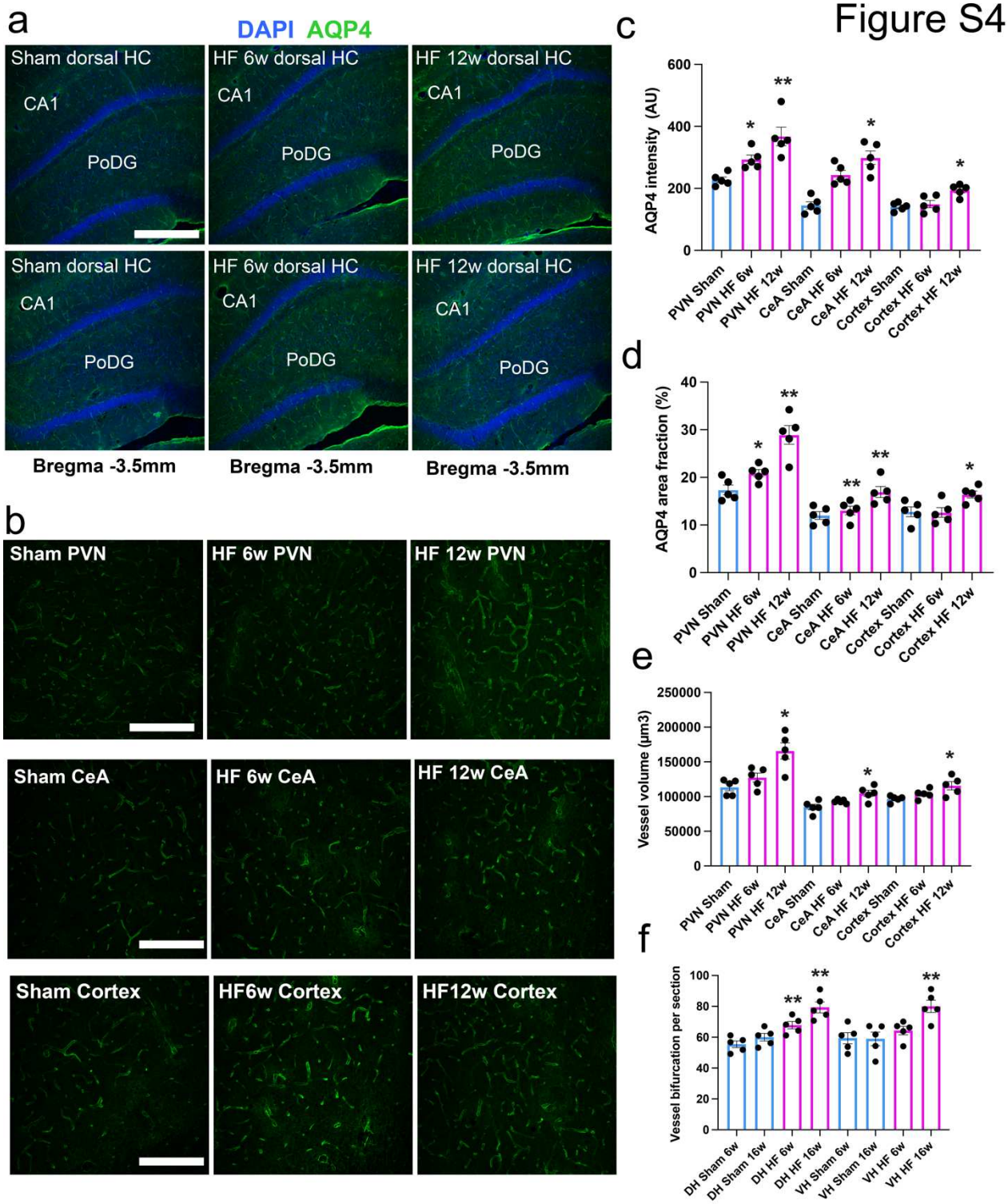

Figure S4 a Representative confocal images of vascularization of the DH in sham and HF rats at different time points. CA1 = cornu ammonis 1, PoDG = polymorph layer of dentate gyrus. **b** Confocal images of AQP-4 labeled vessels in PVN, central amygdala and somatosensory cortex of sham and HF rats. **c-e** Graphs show quantifications for area fraction, signal intensity and vessel volume for PVN and central amygdala at 6- and 12-weeks post-surgery (n=5 animals per group). **f** Quantification of the number of vessel bifurcation points in DH and VH in sham and HF rats (n=5 animals per group). Scale bars 400 µm (a) and 100 µm (b) $p<0.05$*, $p<0.01$** and $p<0.001$***.

Figure S5

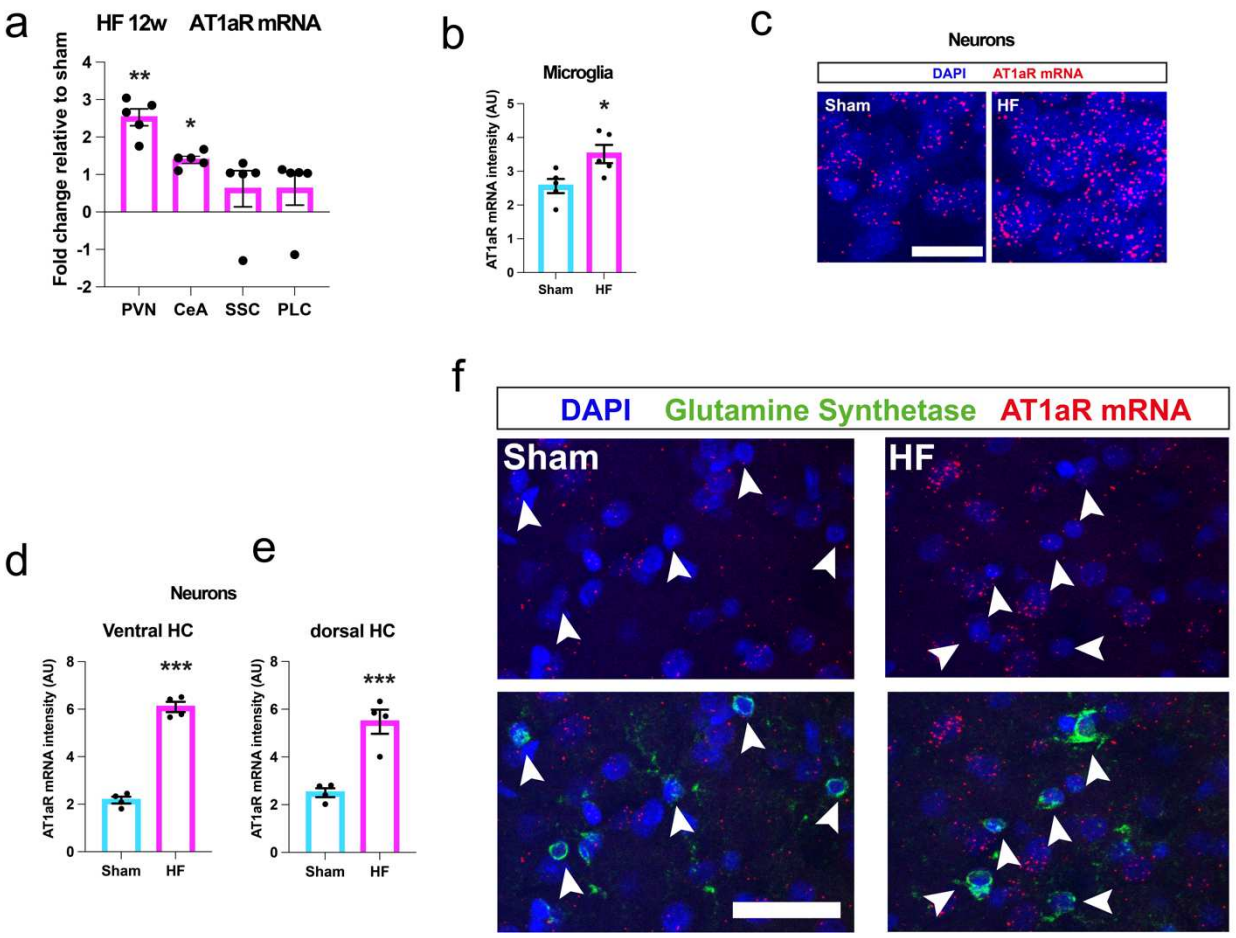

Figure S5 a qPCR for AT1aR in PVN, CeA, SSC and PLC using brain-region specific tissue punches. **b** Graph shows relative AT1aR mRNA intensity in sham and HF microglia (n=5 per group). **c** Confocal images show representative images of AT1aR mRNA signal in hippocampal neurons of sham and HF rats. **d, e** Neurons in the dorsal and ventral hippocampus express significantly more AT1aRs in HF rats (n=4 per group). **f** Hippocampal astrocytes (stained with glutamine synthetase, green) in sham and HF rats do not express AT1aRs. White arrowheads indicate absence of AT1aR mRNA (red). Scale bars 25µm (b) and 50µm (e). $p<0.05$*, $p<0.01$** and $p<0.001$***.

Figure S6

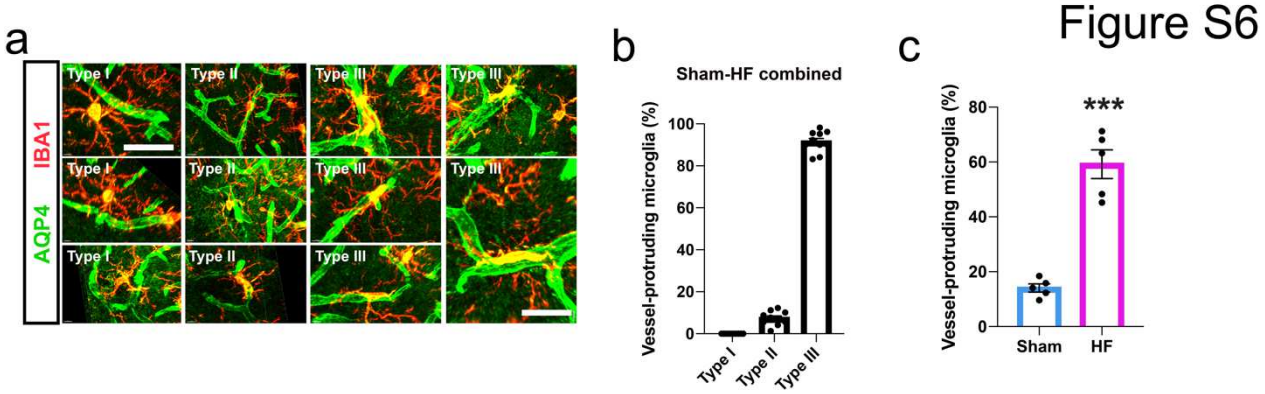

Figure S6 a Representative images of Type I-III microglia in DH of a HF rat. Scale bars 10μm (top left) and 5μm (bottom right). **b** Type III microglia frequently protrude blood vessels in both sham and HF rats (n=5 per group). **c** HF rats have a significantly higher number of vessel-protruding microglia (n=5 per group). $p<0.05$*, $p<0.01$** and $p<0.001$***.

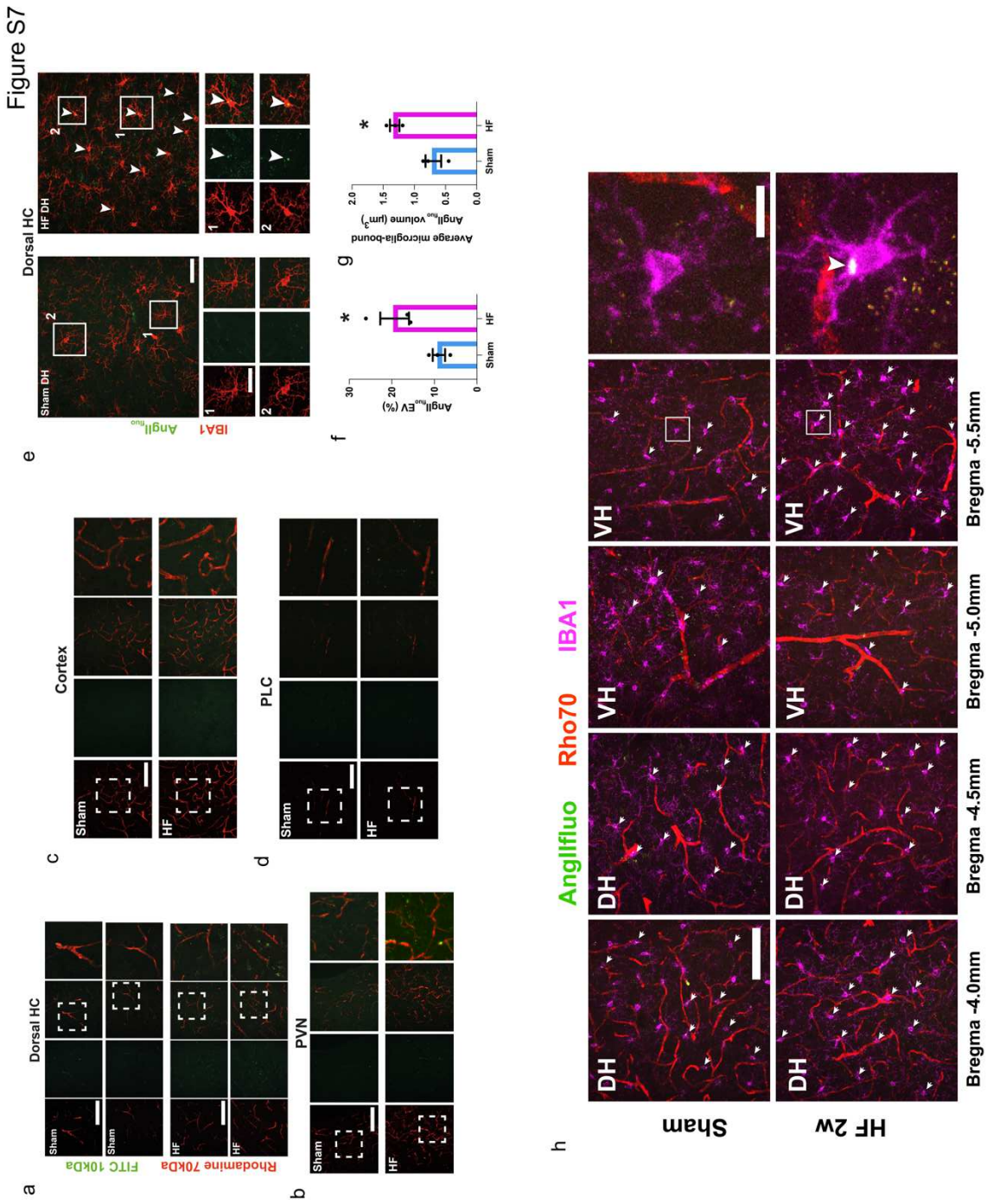

Figure S7 Infusion of intra-carotid fluorescently-labeled dextran dyes for the assessment of BBB integrity. Panels show confocal images of co-infusion of Rho70 and FITC10 in the DH (**a**), PVN (**b**) somatosensory cortex (**c**) and PLC (**d**). **e** Confocal images show DH brain sections from sham and HF rats infused with $AngII_{fluo}$ and counter-stained with IBA1. Insets show high magnification microglia negative (sham, left) and positive (HF, right) for $AngII_{fluo}$. White arrowhead indicates overlap of IBA1 and $AngII_{fluo}$. **f** Quantification of leaked extravasated (EV) $AngII_{fluo}$ in sham and HF rats (n=3 per group). **g** Assessment of microglia-bound $AngII_{fluo}$ in sham and HF rats (n=3 per group). **h** Confocal images show increased co-localization of $AngII_{fluo}$ with IBA1-positive (yellow merge) microglia in DH and VH of HF rats co-infused with Rho70 and $AngII_{fluo}$. White arrowheads indicate overlap of $AngII_{fluo}$ and IBA1 immunosignal. High magnification images show microglia negative (sham, top) and positive (HF, bottom) for $AngII_{fluo}$. Scale bars 150μm (a, b, c, d), 50μm (e), 25μm (e) and 75μm (h). $p<0.05$*.

Figure S8

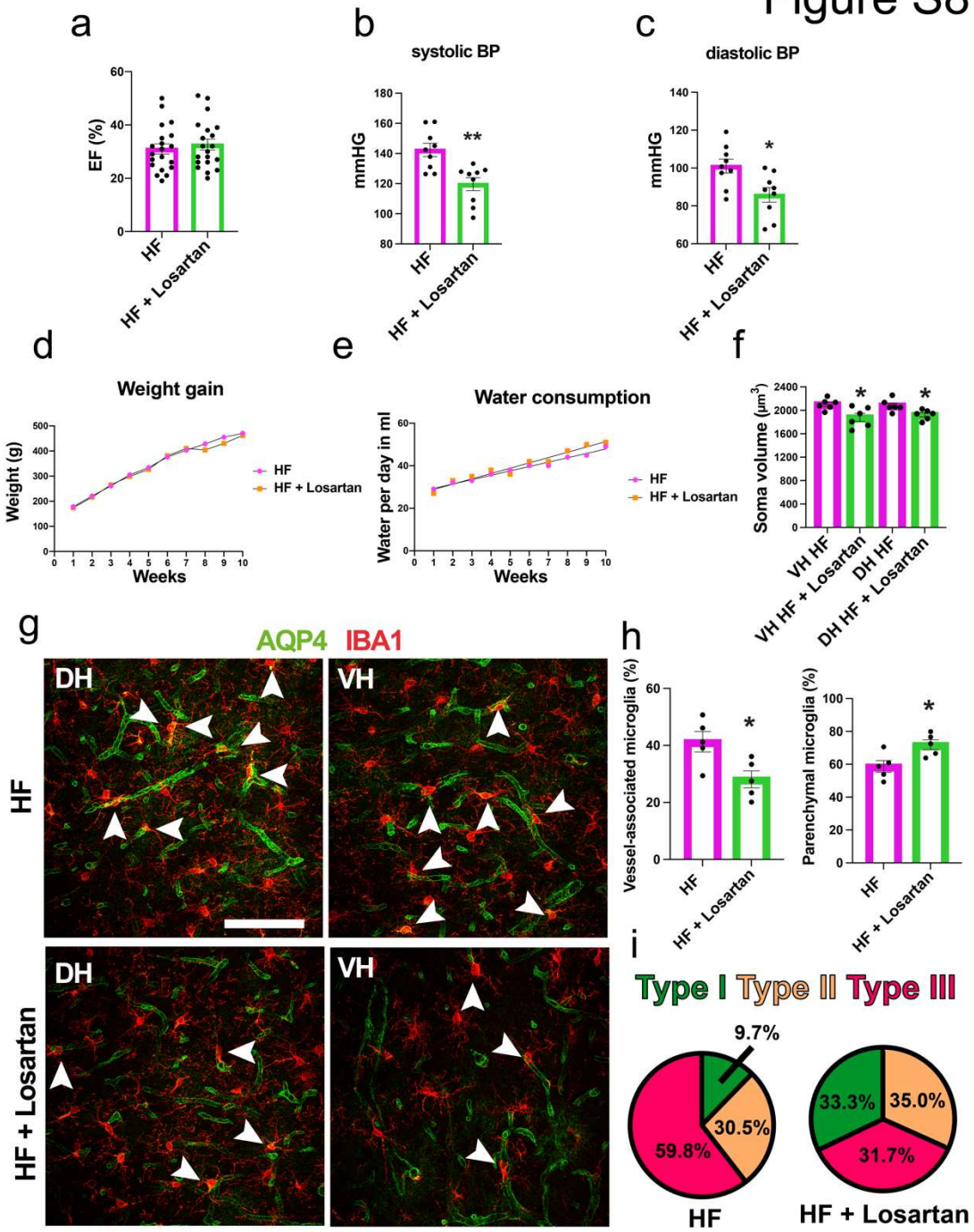

Figure S8 a Summary data for ejection fraction for HF and HF + Losartan experimental groups (n=19 HF, n=22 HF + Losartan). **b, c** Systolic and diastolic blood pressure for HF and HF + Losartan animals assessed via tail-cuff test (n=9 HF, n=9 HF + Losartan). **d** Comparison of weight gain over time between HF and HF+ Losartan animals (n=19 HF, n=22 HF + Losartan). **e** Comparison of water consumption over time between HF and HF + Losartan animals (n=19 HF, n=22 HF + Losartan). **f** Graph shows significant differences in astrocyte soma volume in HF and Losartan treated rats for DH and VH (n=6 per group). **g** Confocal images of IBA1 stained microglia in the vicinity of AQP4-labeled blood vessels in VH and DH of HF and HF + Losartan groups. White arrowheads indicate vessel-associated microglia. **h** Quantification of vessel-associated and parenchymal microglia in HF and HF + Losartan rats (n=5 per group). **i** Quantification of Type I-III vessel-associated microglia in HF and HF + Losartan rats (n=5 per group). Scale bar 100µm (g). $p<0.05$*, $p<0.01$** and $p<0.001$***.

References

1 Groenewegen, A., Rutten, F. H., Mosterd, A. & Hoes, A. W. Epidemiology of heart failure. *Eur J Heart Fail* **22**, 1342-1356, doi:10.1002/ejhf.1858 (2020).

2 Konstam, V., Moser, D. K. & De Jong, M. J. Depression and anxiety in heart failure. *J Card Fail* **11**, 455-463, doi:10.1016/j.cardfail.2005.03.006 (2005).

3 Hammond, C. A. *et al.* Long-Term Cognitive Decline After Newly Diagnosed Heart Failure: Longitudinal Analysis in the CHS (Cardiovascular Health Study). *Circ Heart Fail* **11**, e004476, doi:10.1161/CIRCHEARTFAILURE.117.004476 (2018).

4 Metra, M. & Teerlink, J. R. Heart failure. *Lancet* **390**, 1981-1995, doi:10.1016/S0140-6736(17)31071-1 (2017).

5 Teerlink, J. R., Pfeffer, J. M. & Pfeffer, M. A. Progressive ventricular remodeling in response to diffuse isoproterenol-induced myocardial necrosis in rats. *Circ Res* **75**, 105-113, doi:10.1161/01.res.75.1.105 (1994).

6 Sun, X. Q., Abbate, A. & Bogaard, H. J. Role of cardiac inflammation in right ventricular failure. *Cardiovasc Res* **113**, 1441-1452, doi:10.1093/cvr/cvx159 (2017).

7 Potapenko, E. S., Biancardi, V. C., Zhou, Y. & Stern, J. E. Astrocytes modulate a postsynaptic NMDA-GABAA-receptor crosstalk in hypothalamic neurosecretory neurons. *J Neurosci* **33**, 631-640, doi:10.1523/JNEUROSCI.3936-12.2013 (2013).

8 Diaz, H. S., Toledo, C., Andrade, D. C., Marcus, N. J. & Rio, R. D. Neuroinflammation in heart failure: NEW insights for an old disease. *J Physiol*, doi:10.1113/JP278864 (2019).

9 Bird, C. M. & Burgess, N. The hippocampus and memory: insights from spatial processing. *Nat Rev Neurosci* **9**, 182-194, doi:10.1038/nrn2335 (2008).

10 Strange, B. A., Witter, M. P., Lein, E. S. & Moser, E. I. Functional organization of the hippocampal longitudinal axis. *Nat Rev Neurosci* **15**, 655-669, doi:10.1038/nrn3785 (2014).

11 Mota, C. *et al.* Structural and molecular correlates of cognitive aging in the rat. *Sci Rep* **9**, 2005, doi:10.1038/s41598-019-39645-w (2019).

12 Allen, G. *et al.* Reduced hippocampal functional connectivity in Alzheimer disease. *Arch Neurol* **64**, 1482-1487, doi:10.1001/archneur.64.10.1482 (2007).

13 Suzuki, H. *et al.* Structural abnormality of the hippocampus associated with depressive symptoms in heart failure rats. *Neuroimage* **105**, 84-92, doi:10.1016/j.neuroimage.2014.10.040 (2015).

14 Woo, M. A. *et al.* Regional hippocampal damage in heart failure. *Eur J Heart Fail* **17**, 494-500, doi:10.1002/ejhf.241 (2015).

15 Abe, H., Semba, H. & Takeda, N. The Roles of Hypoxia Signaling in the Pathogenesis of Cardiovascular Diseases. *J Atheroscler Thromb* **24**, 884-894, doi:10.5551/jat.RV17009 (2017).

16 Giordano, F. J. Oxygen, oxidative stress, hypoxia, and heart failure. *J Clin Invest* **115**, 500-508, doi:10.1172/JCI24408 (2005).

17 Althammer, F. *et al.* Three-dimensional morphometric analysis reveals time-dependent structural changes in microglia and astrocytes in the central amygdala and hypothalamic paraventricular nucleus of heart failure rats. *J Neuroinflammation* **17**, 221, doi:10.1186/s12974-020-01892-4 (2020).

18 Najjar, F., Ahmad, M., Lagace, D. & Leenen, F. H. H. Role of Myocardial Infarction-Induced Neuroinflammation for Depression-Like Behavior and Heart Failure in Ovariectomized Female Rats. *Neuroscience* **415**, 201-214, doi:10.1016/j.neuroscience.2019.07.017 (2019).
19 Yu, Y., Wei, S. G., Weiss, R. M. & Felder, R. B. Angiotensin II Type 1a Receptors in the Subfornical Organ Modulate Neuroinflammation in the Hypothalamic Paraventricular Nucleus in Heart Failure Rats. *Neuroscience* **381**, 46-58, doi:10.1016/j.neuroscience.2018.04.012 (2018).
20 Liddelow, S. A. *et al.* Neurotoxic reactive astrocytes are induced by activated microglia. *Nature* **541**, 481-487, doi:10.1038/nature21029 (2017).
21 Cserep, C. *et al.* Microglia monitor and protect neuronal function through specialized somatic purinergic junctions. *Science* **367**, 528-537, doi:10.1126/science.aax6752 (2020).
22 Zucker, I. H. *et al.* The origin of sympathetic outflow in heart failure: the roles of angiotensin II and nitric oxide. *Prog Biophys Mol Biol* **84**, 217-232, doi:10.1016/j.pbiomolbio.2003.11.010 (2004).
23 Zucker, I. H., Xiao, L. & Haack, K. K. The central renin-angiotensin system and sympathetic nerve activity in chronic heart failure. *Clin Sci (Lond)* **126**, 695-706, doi:10.1042/CS20130294 (2014).
24 Huang, B. S. & Leenen, F. H. The brain renin-angiotensin-aldosterone system: a major mechanism for sympathetic hyperactivity and left ventricular remodeling and dysfunction after myocardial infarction. *Curr Heart Fail Rep* **6**, 81-88, doi:10.1007/s11897-009-0013-9 (2009).
25 Phillips, M. I. & Kagiyama, S. Angiotensin II as a pro-inflammatory mediator. *Curr Opin Investig Drugs* **3**, 569-577 (2002).
26 Kang, Y. M. *et al.* Cross-talk between cytokines and renin-angiotensin in hypothalamic paraventricular nucleus in heart failure: role of nuclear factor-kappaB. *Cardiovasc Res* **79**, 671-678, doi:10.1093/cvr/cvn119 (2008).
27 Pyner, S. The paraventricular nucleus and heart failure. *Exp Physiol* **99**, 332-339, doi:10.1113/expphysiol.2013.072678 (2014).
28 Stern, J. E. *et al.* Astrocytes Contribute to Angiotensin II Stimulation of Hypothalamic Neuronal Activity and Sympathetic Outflow. *Hypertension* **68**, 1483-1493, doi:10.1161/HYPERTENSIONAHA.116.07747 (2016).
29 Zheng, H., Li, Y. F., Wang, W. & Patel, K. P. Enhanced angiotensin-mediated excitation of renal sympathetic nerve activity within the paraventricular nucleus of anesthetized rats with heart failure. *Am J Physiol Regul Integr Comp Physiol* **297**, R1364-1374, doi:10.1152/ajpregu.00149.2009 (2009).
30 Biancardi, V. C., Stranahan, A. M., Krause, E. G., de Kloet, A. D. & Stern, J. E. Cross talk between AT1 receptors and Toll-like receptor 4 in microglia contributes to angiotensin II-derived ROS production in the hypothalamic paraventricular nucleus. *Am J Physiol Heart Circ Physiol* **310**, H404-415, doi:10.1152/ajpheart.00247.2015 (2016).
31 Biancardi, V. C., Son, S. J., Ahmadi, S., Filosa, J. A. & Stern, J. E. Circulating angiotensin II gains access to the hypothalamus and brain stem during hypertension via breakdown of the blood-brain barrier. *Hypertension* **63**, 572-579, doi:10.1161/HYPERTENSIONAHA.113.01743 (2014).

32 Biancardi, V. C. & Stern, J. E. Compromised blood-brain barrier permeability: novel mechanism by which circulating angiotensin II signals to sympathoexcitatory centres during hypertension. *J Physiol* **594**, 1591-1600, doi:10.1113/JP271584 (2016).

33 Sun, H. *et al.* Angiotensin II and its receptor in activated microglia enhanced neuronal loss and cognitive impairment following pilocarpine-induced status epilepticus. *Mol Cell Neurosci* **65**, 58-67, doi:10.1016/j.mcn.2015.02.014 (2015).

34 Francis, J., Weiss, R. M., Wei, S. G., Johnson, A. K. & Felder, R. B. Progression of heart failure after myocardial infarction in the rat. *Am J Physiol Regul Integr Comp Physiol* **281**, R1734-1745, doi:10.1152/ajpregu.2001.281.5.R1734 (2001).

35 Parent, M. B. *et al.* Heart Failure Impairs Mood and Memory in Male Rats and down-Regulates the Expression of Numerous Genes Important for Synaptic Plasticity in Related Brain Regions. *Behav Brain Res*, 113452, doi:10.1016/j.bbr.2021.113452 (2021).

36 Toledo, C. *et al.* Cognitive impairment in heart failure is associated with altered Wnt signaling in the hippocampus. *Aging (Albany NY)* **11**, 5924-5942, doi:10.18632/aging.102150 (2019).

37 Prinz, M., Jung, S. & Priller, J. Microglia Biology: One Century of Evolving Concepts. *Cell* **179**, 292-311, doi:10.1016/j.cell.2019.08.053 (2019).

38 Sofroniew, M. V. & Vinters, H. V. Astrocytes: biology and pathology. *Acta Neuropathol* **119**, 7-35, doi:10.1007/s00401-009-0619-8 (2010).

39 Escartin, C. *et al.* Reactive astrocyte nomenclature, definitions, and future directions. *Nat Neurosci* **24**, 312-325, doi:10.1038/s41593-020-00783-4 (2021).

40 Liddelow, S. A. & Barres, B. A. Reactive Astrocytes: Production, Function, and Therapeutic Potential. *Immunity* **46**, 957-967, doi:10.1016/j.immuni.2017.06.006 (2017).

41 Leto, L. & Feola, M. Cognitive impairment in heart failure patients. *J Geriatr Cardiol* **11**, 316-328, doi:10.11909/j.issn.1671-5411.2014.04.007 (2014).

42 Zuccala, G. *et al.* Left ventricular dysfunction: a clue to cognitive impairment in older patients with heart failure. *J Neurol Neurosurg Psychiatry* **63**, 509-512, doi:10.1136/jnnp.63.4.509 (1997).

43 Khurana, R., Simons, M., Martin, J. F. & Zachary, I. C. Role of angiogenesis in cardiovascular disease: a critical appraisal. *Circulation* **112**, 1813-1824, doi:10.1161/CIRCULATIONAHA.105.535294 (2005).

44 Mueller, K. *et al.* Brain Damage With Heart Failure: Cardiac Biomarker Alterations and Gray Matter Decline. *Circ Res* **126**, 750-764, doi:10.1161/CIRCRESAHA.119.315813 (2020).

45 Skuli, N. *et al.* Endothelial HIF-2alpha regulates murine pathological angiogenesis and revascularization processes. *J Clin Invest* **122**, 1427-1443, doi:10.1172/JCI57322 (2012).

46 Befani, C. & Liakos, P. The role of hypoxia-inducible factor-2 alpha in angiogenesis. *J Cell Physiol* **233**, 9087-9098, doi:10.1002/jcp.26805 (2018).

47 Biancardi, V. C. & Stern, J. Angiotensin II contributes to microglial cell activation in the PVN of hypertensive rats. *The FASEB Journal* **27:1** supplement, 699.618-699.618 (2013).

48 Haruwaka, K. *et al.* Dual microglia effects on blood brain barrier permeability induced by systemic inflammation. *Nat Commun* **10**, 5816, doi:10.1038/s41467-019-13812-z (2019).

49 Ballabh, P., Braun, A. & Nedergaard, M. The blood-brain barrier: an overview: structure, regulation, and clinical implications. *Neurobiol Dis* **16**, 1-13, doi:10.1016/j.nbd.2003.12.016 (2004).

50 Halder, S. K. & Milner, R. Mild hypoxia triggers transient blood-brain barrier disruption: a fundamental protective role for microglia. *Acta Neuropathol Commun* **8**, 175, doi:10.1186/s40478-020-01051-z (2020).
51 Fanselow, M. S. & Dong, H. W. Are the dorsal and ventral hippocampus functionally distinct structures? *Neuron* **65**, 7-19, doi:10.1016/j.neuron.2009.11.031 (2010).
52 Broadbent, N. J., Squire, L. R. & Clark, R. E. Spatial memory, recognition memory, and the hippocampus. *Proc Natl Acad Sci U S A* **101**, 14515-14520, doi:10.1073/pnas.0406344101 (2004).
53 Mbakwem, A., Aina, F. & Amadi, C. Expert Opinion-Depression in Patients with Heart Failure: Is Enough Being Done? *Card Fail Rev* **2**, 110-112, doi:10.15420/cfr.2016:21:1 (2016).
54 Parissis, J. T., Fountoulaki, K., Paraskevaidis, I. & Kremastinos, D. Depression in chronic heart failure: novel pathophysiological mechanisms and therapeutic approaches. *Expert Opin Investig Drugs* **14**, 567-577, doi:10.1517/13543784.14.5.567 (2005).
55 Rustad, J. K., Stern, T. A., Hebert, K. A. & Musselman, D. L. Diagnosis and treatment of depression in patients with congestive heart failure: a review of the literature. *Prim Care Companion CNS Disord* **15**, doi:10.4088/PCC.13r01511 (2013).
56 Rutledge, T., Reis, V. A., Linke, S. E., Greenberg, B. H. & Mills, P. J. Depression in heart failure a meta-analytic review of prevalence, intervention effects, and associations with clinical outcomes. *J Am Coll Cardiol* **48**, 1527-1537, doi:10.1016/j.jacc.2006.06.055 (2006).
57 Frey, A. *et al.* Experimental heart failure causes depression-like behavior together with differential regulation of inflammatory and structural genes in the brain. *Front Behav Neurosci* **8**, 376, doi:10.3389/fnbeh.2014.00376 (2014).
58 Prickaerts, J., Raaijmakers, W. & Blokland, A. Effects of myocardial infarction and captopril therapy on anxiety-related behaviors in the rat. *Physiol Behav* **60**, 43-50 (1996).
59 Schoemaker, R. G. & Smits, J. F. Behavioral changes following chronic myocardial infarction in rats. *Physiol Behav* **56**, 585-589 (1994).
60 Tang, M. *et al.* Hippocampal proteomic changes of susceptibility and resilience to depression or anxiety in a rat model of chronic mild stress. *Transl Psychiatry* **9**, 260, doi:10.1038/s41398-019-0605-4 (2019).
61 Nimmerjahn, A., Kirchhoff, F. & Helmchen, F. Resting microglial cells are highly dynamic surveillants of brain parenchyma in vivo. *Science* **308**, 1314-1318, doi:10.1126/science.1110647 (2005).
62 Torres-Platas, S. G. *et al.* Morphometric characterization of microglial phenotypes in human cerebral cortex. *J Neuroinflammation* **11**, 12, doi:10.1186/1742-2094-11-12 (2014).
63 Davis, B. M., Salinas-Navarro, M., Cordeiro, M. F., Moons, L. & De Groef, L. Characterizing microglia activation: a spatial statistics approach to maximize information extraction. *Sci Rep* **7**, 1576, doi:10.1038/s41598-017-01747-8 (2017).
64 Guttenplan, K. A. *et al.* Neurotoxic reactive astrocytes induce cell death via saturated lipids. *Nature*, doi:10.1038/s41586-021-03960-y (2021).
65 de Kloet, A. D., Liu, M., Rodriguez, V., Krause, E. G. & Sumners, C. Role of neurons and glia in the CNS actions of the renin-angiotensin system in cardiovascular control. *Am J*

Physiol Regul Integr Comp Physiol **309**, R444-458, doi:10.1152/ajpregu.00078.2015 (2015).

66 Iulita, M. F. *et al.* Differential effect of angiotensin II and blood pressure on hippocampal inflammation in mice. *J Neuroinflammation* **15**, 62, doi:10.1186/s12974-018-1090-z (2018).

67 Benicky, J. *et al.* Angiotensin II AT1 receptor blockade ameliorates brain inflammation. *Neuropsychopharmacology* **36**, 857-870, doi:10.1038/npp.2010.225 (2011).

68 Bisht, K. *et al.* Capillary-associated microglia regulate vascular structure and function through PANX1-P2RY12 coupling in mice. *Nat Commun* **12**, 5289, doi:10.1038/s41467-021-25590-8 (2021).

69 Mowry, F. E., Peaden, S. C., Stern, J. E. & Biancardi, V. C. TLR4 and AT1R mediate blood-brain barrier disruption, neuroinflammation, and autonomic dysfunction in spontaneously hypertensive rats. *Pharmacol Res*, 105877, doi:10.1016/j.phrs.2021.105877 (2021).

70 Zhao, Z., Nelson, A. R., Betsholtz, C. & Zlokovic, B. V. Establishment and Dysfunction of the Blood-Brain Barrier. *Cell* **163**, 1064-1078, doi:10.1016/j.cell.2015.10.067 (2015).

71 Chen, W. W., Zhang, X. & Huang, W. J. Role of neuroinflammation in neurodegenerative diseases (Review). *Mol Med Rep* **13**, 3391-3396, doi:10.3892/mmr.2016.4948 (2016).

72 Phatnani, H. & Maniatis, T. Astrocytes in neurodegenerative disease. *Cold Spring Harb Perspect Biol* **7**, doi:10.1101/cshperspect.a020628 (2015).

73 Yang, Y. & Torbey, M. T. Angiogenesis and Blood-Brain Barrier Permeability in Vascular Remodeling after Stroke. *Curr Neuropharmacol* **18**, 1250-1265, doi:10.2174/1570159X18666200720173316 (2020).

74 Biancardi, V. C. *et al.* Contribution of central nervous system endothelial nitric oxide synthase to neurohumoral activation in heart failure rats. *Hypertension* **58**, 454-463, doi:10.1161/HYPERTENSIONAHA.111.175810 (2011).

75 Tang, Y. *et al.* Social touch promotes interfemale communication via activation of parvocellular oxytocin neurons. *Nat Neurosci* **23**, 1125-1137, doi:10.1038/s41593-020-0674-y (2020).

76 Daugherty, A., Rateri, D., Hong, L. & Balakrishnan, A. Measuring blood pressure in mice using volume pressure recording, a tail-cuff method. *J Vis Exp*, doi:10.3791/1291 (2009).

77 Lalonde, R. The neurobiological basis of spontaneous alternation. *Neurosci Biobehav Rev* **26**, 91-104, doi:10.1016/s0149-7634(01)00041-0 (2002).

78 McGaugh, J. L. The amygdala modulates the consolidation of memories of emotionally arousing experiences. *Annu Rev Neurosci* **27**, 1-28, doi:10.1146/annurev.neuro.27.070203.144157 (2004).